Inorganic Chemistry

Article

pubs.acs.org/IC

Xenon(IV)−Carbon Bond of $[C_6F_5XeF_2]^+$; Structural Characterization and Bonding of $[C_6F_5XeF_2][BF_4]$, $[C_6F_5XeF_2][BF_4]\cdot 2HF$, and $[C_6F_5XeF_2][BF_4]\cdot n NCCH_3$ (n = 1, 2); and the Fluorinating Properties of $[C_6F_5XeF_2][BF_4]$

Karsten Koppe,[†,‡,§,⊥] Jamie Haner,[‡,⊥] Hélène P. A. Mercier,[‡] Hermann-J. Frohn,*[,†] and Gary J. Schrobilgen*[,‡]

[†]Inorganic Chemistry, Universität Duisburg-Essen, Lotharstraße 1, D-47048 Duisburg, Germany

[‡]Department of Chemistry, McMaster University, Hamilton, Ontario L8S 4M1, Canada

Supporting Information

ABSTRACT: The $[C_6F_5XeF_2]^+$ cation is the only example of a Xe^{IV}−C bond, which had only been previously characterized as its $[BF_4]^-$ salt in solution by multi-NMR spectroscopy. The $[BF_4]^-$ salt and its new CH_3CN and HF solvates, $[C_6F_5XeF_2][BF_4]\cdot 1.5CH_3CN$ and $[C_6F_5XeF_2][BF_4]\cdot 2HF$, have now been synthesized and fully characterized in the solid state by low-temperature, single-crystal X-ray diffraction and Raman spectroscopy. Crystalline $[C_6F_5XeF_2][BF_4]$ and $[C_6F_5XeF_2][BF_4]\cdot 1.5CH_3CN$ were obtained from CH_3CN/CH_2Cl_2 solvent mixtures, and $[C_6F_5XeF_2][BF_4]\cdot 2HF$ was obtained from anhydrous HF (aHF), where $[C_6F_5XeF_2][BF_4]\cdot 1.5CH_3CN$ is comprised of an equimolar mixture of $[C_6F_5XeF_2][BF_4]\cdot CH_3CN$ and $[C_6F_5XeF_2][BF_4]\cdot 2CH_3CN$. The crystal structures show that the $[C_6F_5XeF_2]^+$ cation has two short contacts with the F atoms of $[BF_4]^-$ or with the F or N atoms of the solvent molecules, HF and CH_3CN. The low-temperature solid-state Raman spectra of $[C_6F_5XeF_2][BF_4]$ and $C_6F_5IF_2$ were assigned with the aid of quantum-chemical calculations. The bonding in $[C_6F_5XeF_2]^+$, $C_6F_5IF_2$, $[C_6F_5XeF_2][BF_4]$, $[C_6F_5XeF_2][BF_4]\cdot CH_3CN$, $[C_6F_5XeF_2][BF_4]\cdot 2CH_3CN$, and $[C_6F_5XeF_2][BF_4]\cdot 2HF$ was assessed with the aid of natural bond orbital analyses and molecular orbital calculations. The ^{129}Xe, ^{19}F, and ^{11}B NMR spectra of $[C_6F_5XeF_2][BF_4]$ in aHF are reported and compared with the ^{19}F NMR spectrum of $C_6F_5IF_2$, and all previously unreported $J(^{129}Xe-^{19}F)$ and $J(^{19}F-^{19}F)$ couplings were determined. The long-term solution stabilities of $[C_6F_5XeF_2][BF_4]$ were investigated by ^{19}F NMR spectroscopy and the oxidative fluorinating properties of $[C_6F_5XeF_2][BF_4]$ were demonstrated by studies of its reactivity with $K[C_6F_5BF_3]$, $Pn(C_6F_5)_3$ (Pn = P, As, or Bi), and C_6F_5X (X = Br or I).

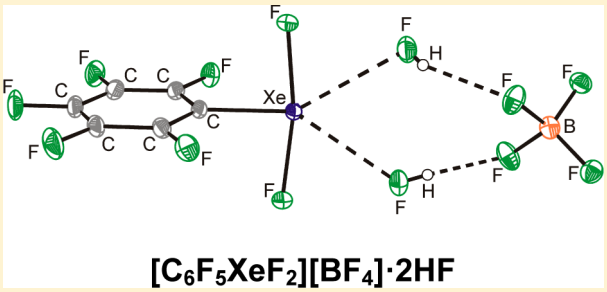

INTRODUCTION

The majority of the known Xe(IV) compounds are stabilized by oxidatively resistant F or O atoms, or by polyatomic, highly electronegative O-bonded groups. These are exemplified by XeF_4,[1−3] $[XeF_3]^+$,[4−6] $[XeF_5]^-$,[7] $XeOF_2$,[8−11] $[XeOF_3]^-$,[11,12] XeO_2,[13] $Xe(OTeF_5)_4$,[14,15] $Xe(OTeF_5)_{4-x}F_x$ (x = 1−3),[2] $[F_xXe(OTeF_5)_{3-x}]^+$ (x = 0−2),[16] $F_3XeOIOF_4$,[17] and the XeF_4 coordination compound $[Mg(XeF_2)(XeF_4)][AsF_6]_2$.[18] Xenon(IV) chemistry has experienced a resurgence in the areas of oxide and oxide fluoride compounds in recent years.[8,12,13,19,20] Most recently, the mixed oxidation state Xe(IV)/Xe(II) oxide fluoride cations $[(XeOF_2)_nXeF]^+$ (n = 1, 2),[20] and the first Xe(IV) hydroxy derivatives, namely, $[HOXeF_2]^+$ and $[HOXeF_2OXeF_2]^+$, have been described.[20] The aforementioned studies have also led to the discovery of a number of new bonding modalities such as the first Xe^{IV}−N bond in the donor−acceptor adduct $XeOF_2\cdot CH_3CN$;[8] the first examples of AX_5E_2 and AX_3YE_2 valence shell electron pair repulsion (VSEPR) arrangements, $[XeF_5]^-$[7] and $[XeOF_3]^-$;[12] the missing oxide of Xe(IV), XeO_2;[13] and the only example of HF coordinated to Xe(IV), which was observed in the crystal structure of $[XeF_3][Sb_2F_{11}]\cdot HF$.[20]

An impressive variety of Xe^{II}−C-bonded compounds are now known, which include not only xenonium salts having the formulations [RXe][A] (R = aryl,[21−23] alkenyl,[24−26] and alkynyl,[27−29] A = anion) but also neutral $XeAr_2$ and ArXeZ (Ar = aryl, Z = F or Cl) species, which are exemplified by $Xe(C_6F_5)_2$,[30−33] C_6F_5XeCl,[34] and C_6F_5XeF.[35] More recently, the syntheses of the dicationic salt, $[XeC_6F_4Xe][BF_4]_2$, and the zwitterionic compound, $XeC_6F_4BF_3$, along with their solution characterizations by ^{13}C, ^{19}F, and ^{129}Xe NMR spectroscopy, were reported.[36]

Received: July 29, 2014

   dx.doi.org/10.1021/ic501831j | Inorg. Chem. XXXX, XXX, XXX−XXX

The oxidative strength of the parent Xe(IV) fluoride, XeF_4, is much greater than that of XeF_2, and the fluoride ion donor strength of XeF_4 is less than that of XeF_2 or XeF_6.[37] Consequently, a suitable organic ligand and corresponding ligand transfer reagent for the formation of a Xe^{IV}–C bond must be oxidatively robust.

The synthesis and characterization by low-temperature solution ^{11}B, ^{13}C, ^{19}F, and ^{129}Xe NMR spectroscopy of the first compound to contain a Xe^{IV}–C bond, $[C_6F_5XeF_2][BF_4]$, was reported in a prior communication.[38] The substitution of a fluorine atom of XeF_4 by an organic ligand was achieved by reaction of XeF_4 with $C_6F_5BF_2$ in CH_2Cl_2 at −55 °C (Scheme 1).[38] The ensuing xenodeborylation reaction likely occurs by

Scheme 1. Proposed Xenodeborylation[21,22] Mechanism for the Formation of $[C_6F_5XeF_2][BF_4]$

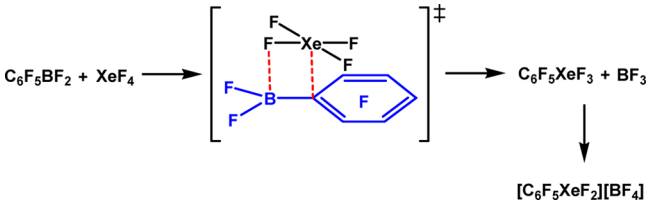

polarization of an Xe–F bond by the Lewis acid $C_6F_5BF_2$ without complete fluoride ion abstraction. As a result of this acid–base interaction, the C_6F_5 group acquires more nucleophilic character and migrates to the electrophilic Xe(IV) center.[21,22] In a final step, fluoride abstraction from the XeF_3 group of $C_6F_5XeF_3$ by BF_3 yields $[C_6F_5XeF_2][BF_4]$ (Scheme 1).

Although the ^{11}B, ^{13}C, ^{19}F, and ^{129}Xe NMR spectra of $[C_6F_5XeF_2][BF_4]$ in CH_3CN/CD_3CN at −40 °C were reported in a preliminary communication,[38] the $J(^{19}F-^{19}F)$ coupling constants of the C_6F_5 group, the $J(^{19}F-^{129}Xe)$ couplings involving aryl fluorine nuclei, and the $J(^{13}C-^{129}Xe)$ couplings were not reported. The ability of $[C_6F_5XeF_2]^+$ to oxidatively fluorinate $P(C_6F_5)_3$, C_6F_5I, and I_2 in CH_3CN solutions to $P(C_6F_5)_3F_2$, $C_6F_5IF_2$, and IF_5, respectively, was demonstrated in the preliminary work.[38]

Since its discovery, the $[C_6F_5XeF_2]^+$ cation had not been structurally characterized in the solid state by single-crystal X-ray diffraction or by vibrational spectroscopy, and no computational studies leading to a detailed description of its bonding have been forthcoming. The present paper provides an improved synthesis of $[C_6F_5XeF_2][BF_4]$ in high purity and yield as well as the detailed characterization of this salt and its solvates, namely, $[C_6F_5XeF_2][BF_4]\cdot 1.5CH_3CN$ and $[C_6F_5XeF_2][BF_4]\cdot 2HF$, by low-temperature single-crystal X-ray diffraction and Raman spectroscopy. Quantum-chemical calculations were employed to arrive at detailed assignments of the Raman spectra of the $[C_6F_5XeF_2]^+$ cation and of isoelectronic $C_6F_5IF_2$ and to assess and compare the bonding in both species. Improved ^{129}Xe, ^{19}F, and ^{11}B NMR spectra of $[C_6F_5XeF_2][BF_4]$ in CH_3CN and anhydrous HF (aHF) are reported, and the complex ^{19}F NMR spectra of $[C_6F_5XeF_2][BF_4]$ and $C_6F_5IF_2$ were simulated to determine all $J(^{19}F-^{19}F)$ and $J(^{19}F-^{129}Xe)$ couplings. The long-term decomposition profiles of $[C_6F_5XeF_2][BF_4]$ solutions in CH_3CN and aHF were assessed, and studies of its fluorinating abilities were extended to its reactions with $K[C_6F_5BF_3]$ in CH_3CN, $Pn(C_6F_5)_3$ (Pn = As, Bi) in CH_3CN and to fluorinations of the fluoroaryl halides, C_6F_5X (X = Br or I) in CH_3CN and aHF.

RESULTS AND DISCUSSION

Syntheses and Stabilities of $[C_6F_5XeF_2]^+$ Salts. *(a) $[C_6F_5XeF_2][BF_4]$ and $[C_6F_5XeF_2][BF_4]\cdot 2HF$.* In the previous[38] and present work, $[C_6F_5XeF_2][BF_4]$ was obtained by reaction of $C_6F_5BF_2$ and XeF_4 in CH_2Cl_2 at −55 °C (eq 1).

$$C_6F_5BF_2 + XeF_4 \xrightarrow[-55\ ^\circ C]{CH_2Cl_2} [C_6F_5XeF_2][BF_4] \quad (1)$$

The present work shows that the synthesis of high-purity $[C_6F_5XeF_2][BF_4]$ in high yield is limited to a narrow concentration range. Unlike the syntheses of organoxenon(II) salts,[21−23] more dilute solutions must be used to obtain optimum yields because of the low solubility of XeF_4 in CH_2Cl_2 at −55 °C (~20 μmol mL^{-1}) and the voluminous nature of the precipitated product, which tends to partially occlude solid XeF_4 and likely inhibits its reaction with $C_6F_5BF_2$. In a typical reaction, XeF_4 (~1 mmol) was partially dissolved, with vigorous stirring, in cold CH_2Cl_2 (−78 °C, 20 mL). A freshly prepared solution of $C_6F_5BF_2$ in CH_2Cl_2 (~7 mL) was added to the XeF_4 suspension at −78 °C. The reaction rate was negligible at this temperature, but accelerated at ca. −60 °C, whereupon $[C_6F_5XeF_2][BF_4]$ rapidly precipitated as a voluminous light yellow solid, resulting in complete reaction after 1 h at −55 °C. Although it was not possible to weigh the product because of its thermal instability, the reaction appears to be nearly quantitative based on the consumption of XeF_4 and Raman and NMR spectroscopic analyses. Syntheses employing smaller quantities of solvent (1–5 mL) resulted in reduced yields (<50%) even with longer reaction times (3 h). In these instances, the separated and washed solids consisted of mixtures containing up to 50 mol% XeF_4. In addition to high dilution, the use of equimolar amounts of XeF_4 and $C_6F_5BF_2$ is essential because excess XeF_4 cannot be effectively removed by multiple washings of $[C_6F_5XeF_2][BF_4]/XeF_4$ mixtures with cold CH_2Cl_2 (−55 °C). The use of a stoichiometric excess of $C_6F_5BF_2$ also resulted in reduced yields. A probable explanation is provided in the Supporting Information (Electrophilic Fluorination Properties of $[C_6F_5XeF_2][BF_4]$).

The solution stability of $[C_6F_5XeF_2][BF_4]$ depends on the nature of the solvent and on the temperature. The $[C_6F_5XeF_2][BF_4]$ salt is insoluble in the weakly coordinating solvents CH_2Cl_2, SO_2ClF, and 1,1,1,3,3-pentafluorobutane (PFB), which is consistent with strongly ion-paired $[C_6F_5XeF_2]^+$ cations and $[BF_4]^-$ anions. Although $[C_6F_5XeF_2][BF_4]$ is a strong oxidant, it is stable as a suspension in CH_2Cl_2 at low temperatures with oxidation taking place at temperatures exceeding −40 °C. Warming of these suspensions to room temperature resulted in rapid gas evolution and formation of a black suspension that contained a mixture of C_6F_5H, C_6F_6, and C_6F_5Cl in a 6:3:1 molar ratio and the fluorination products of CH_2Cl_2, namely, CH_2F_2, CH_2ClF, CHF_3, and HF, in a 78:33:7:75 molar ratio.

The bright yellow-orange crystalline HF solvate, $[C_6F_5XeF_2][BF_4]\cdot 2HF$, was formed by pumping aHF solutions of $[C_6F_5XeF_2][BF_4]$ to dryness under dynamic vacuum at ca. −76 °C, enabling its X-ray crystal structure to be determined (see X-ray Crystal Structures). The color of crystalline $[C_6F_5XeF_2][BF_4]\cdot 2HF$ contrasts with that of $[C_6F_5XeF_2][BF_4]$, which is pale yellow. Conversion of the HF solvate to its parent $[C_6F_5XeF_2][BF_4]$ salt was achieved by dissolution of the solid

dx.doi.org/10.1021/ic501831j | Inorg. Chem. XXXX, XXX, XXX–XXX

in CH_3CN followed by removal of CH_3CN/HF at ca. −40 °C under dynamic vacuum.

(b) Stability of $[C_6F_5XeF_2][BF_4]$ in aHF. Solutions of $[C_6F_5XeF_2][BF_4]$ are more stable in aHF than in the basic solvent, CH_3CN, and can be stored at −78 °C for up to 18 d with negligible decomposition. Complete decomposition occurred within 88 d in aHF at −40 °C, within 4 d at −30 °C, and was very rapid with vigorous gas evolution at room temperature (reaction product distributions are given in Scheme 2). Solutions of $[C_6F_5XeF_2][BF_4]$ in aHF that were

Scheme 2. Decomposition Product Distribution of $[C_6F_5XeF_2][BF_4]$ in aHF[a]

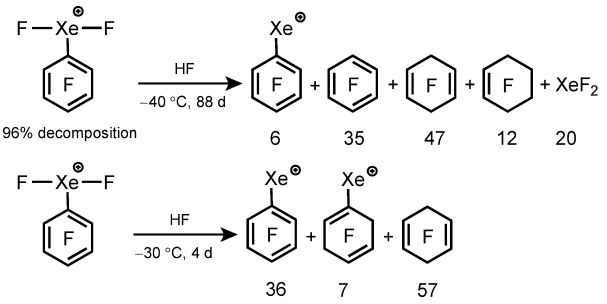

[a]The total weighted ^{19}F NMR intensities of the C_6F_5 groups and their derivatives is set equal to 100 mol%.

allowed to decompose at −40 °C contained XeF_2, C_6F_6, *c*-C_6F_8-1,4, and *c*-C_6F_{10}. The formation of XeF_2 and C_6F_6 (eq 2) may arise from the formal heterolysis of the Xe−C bond of the $[C_6F_5XeF_2]^+$ cation and fluoride addition to the *ipso*-carbon atom of the carbenium ion (Balz−Schiemann-type reaction, eqs 3 and 4).[39] Alternatively, nonionic reductive elimination of the Xe(IV) center in $[C_6F_5XeF_2][BF_4]$ to Xe(II), accompanied by C−F bond formation, could occur.

$$[C_6F_5XeF_2][BF_4] \xrightarrow[\geq -40\ ^\circ C]{aHF} C_6F_6 + XeF_2 + BF_3 \quad (2)$$

$$[ArN_2][BF_4] \rightarrow ArF + N_2 + BF_3 \quad (3)$$

$$[C_6F_5Xe][BF_4] \xrightarrow[20\ ^\circ C,\ 54\ d]{aHF} C_6F_6 + Xe^0 + BF_3 \quad (4)$$

The cyclic olefins, *c*-C_6F_8-1,4 and *c*-C_6F_{10}, likely result from the fluorination of C_6F_6 by XeF_2 and, to a lesser extent, by $[C_6F_5XeF_2][BF_4]$.

Samples that had decomposed at −30 °C contained *c*-C_6F_8-1,4 and the $[BF_4]^-$ salts of $[C_6F_5Xe]^+$ and $[c\text{-}C_6F_7Xe]^+$ (Scheme 2). The formation of *c*-C_6F_8-1,4 and $[c\text{-}C_6F_7Xe]^+$ can be attributed to fluorination of C_6F_6 and the $[C_6F_5Xe]^+$ cation, respectively. No fluorine addition to $[C_6F_5Xe]^+$ occurred with XeF_2 in aHF below −10 °C in the absence of a Lewis acid.[24] However, the oxidative strength of the aHF solution is expected to increase with the formation of the Lewis acid BF_3 as $[C_6F_5XeF_2][BF_4]$ decomposition proceeds (eq 2). Boron trifluoride serves to activate the fluoro-oxidizers XeF_2 and $[C_6F_5XeF_2]^+$, enabling the formation of $[c\text{-}C_6F_7Xe]^+$. The salt, $[C_6F_5XeF_2][BF_4]$, decomposes spontaneously at room temperature in aHF to yield *c*-C_6F_8-1,4 as the major product and small amounts of $[C_6F_5Xe][BF_4]$ and C_6F_6. Overall, *c*-C_6F_8-1,4 formation is the dominant reaction channel at all temperatures that were studied (24, −30, and −40 °C). Heterolytic cleavage of $[C_6F_5XeF_2][BF_4]$ by HF proceeds significantly faster than it does in the case of $[C_6F_5Xe][BF_4]$, which is stable in aHF at room temperature for 12 h and decomposed (eq 4) by only 1.5 and 15% to form C_6F_6 and Xe^0 after 2 and 54 d, respectively.[40]

In conclusion, Xe(IV) in $[C_6F_5XeF_2]^+$ is more strongly electron-withdrawing than Xe(II) in $[C_6F_5Xe]^+$, enabling heterolysis of the strongly polarized Xe^{IV}−C bond in BF_3-acidified aHF. In both cases, heterolytic cleavage of the Xe−C bonds in $[C_6F_5Xe]^+$ and $[C_6F_5XeF_2]^+$ in aHF leads to Xe^0 and XeF_2 formation, respectively.

(c) Stability of $[C_6F_5XeF_2][BF_4]$ in CH_3CN and the Synthesis of $[C_6F_5XeF_2][BF_4]\cdot 1.5NCCH_3$. The decomposition of $[C_6F_5XeF_2][BF_4]$ in CH_3CN solution proceeds slowly at −40 °C. After 58 d, the salt had completely decomposed and was converted to mainly $[C_6F_5Xe]^+$, with smaller amounts of C_6F_6, *c*-C_6F_8-1,4, XeF_2, and HF (Scheme 3). The decomposition was

Scheme 3. Product Distribution for the Decomposition of $[C_6F_5XeF_2][BF_4]$ in CH_3CN (cf. Scheme 2)

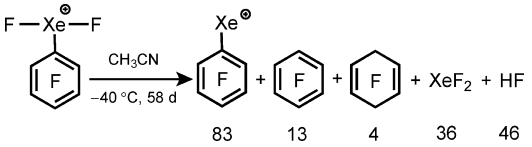

attributed to reduction of R−Xe^{IV} to R−Xe^{II} by the organic solvent. Single crystals of $[C_6F_5XeF_2][BF_4]$ were grown from CH_3CN by slow removal of the solvent under dynamic vacuum at ca. −40 °C.

The $[C_6F_5XeF_2][BF_4]\cdot 1.5CH_3CN$ adduct is only stable at low temperatures (−78 °C). As noted above, pumping on solutions of $[C_6F_5XeF_2][BF_4]$ in CH_3CN above the freezing point of the solvent (ca. −40 °C) does not result in CH_3CN coordination to the electrophilic Xe(IV) center of $[C_6F_5XeF_2][BF_4]$ in the solid state. When solutions of $[C_6F_5XeF_2][BF_4]$ in CH_2Cl_2/CH_3CN mixtures were cooled to and allowed to stand at −78 °C for several days, the more strongly coordinating cosolvent, CH_3CN, slowly crystallized along with yellow crystals of $[C_6F_5XeF_2][BF_4]\cdot 1.5CH_3CN$.

Electrophilic Fluorination Properties of $[C_6F_5XeF_2][BF_4]$. *(a) Reactivity of $[C_6F_5XeF_2][BF_4]$ with $K[C_6F_5BF_3]$.* It is possible that excess $C_6F_5BF_2$ used in the preparation of $[C_6F_5XeF_2][BF_4]$ could further react to form $[C_6F_5XeF_2][C_6F_5BF_3]$, which is presumed to be less stable than $[C_6F_5XeF_2][BF_4]$. The reactivity of $[C_6F_5XeF_2]^+$ toward $[C_6F_5BF_3]^-$ was studied by reacting $[C_6F_5XeF_2][BF_4]$ with suspensions of $K[C_6F_5BF_3]$ in CH_3CN at −40 °C. The main soluble product was $[C_6F_5Xe]^+$ (86) along with C_6F_6 (6), $[C_6F_7BF_3]^-$ (8), XeF_2 (27), and HF (15) (Scheme 4). The products, $[C_6F_5Xe]^+$ and HF, were also detected in the decomposition of $[C_6F_5XeF_2][BF_4]$ in CH_3CN in the absence of $K[C_6F_5BF_3]$. The more rapid reduction of the $[C_6F_5XeF_2]^+$

Scheme 4. Product Distribution Resulting from the Reaction of $[C_6F_5XeF_2][BF_4]$ with a Suspension of $K[C_6F_5BF_3]$ in CH_3CN at −40 °C

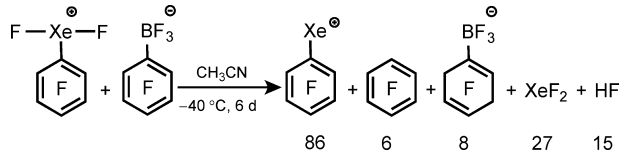

dx.doi.org/10.1021/ic501831j | Inorg. Chem. XXXX, XXX, XXX−XXX

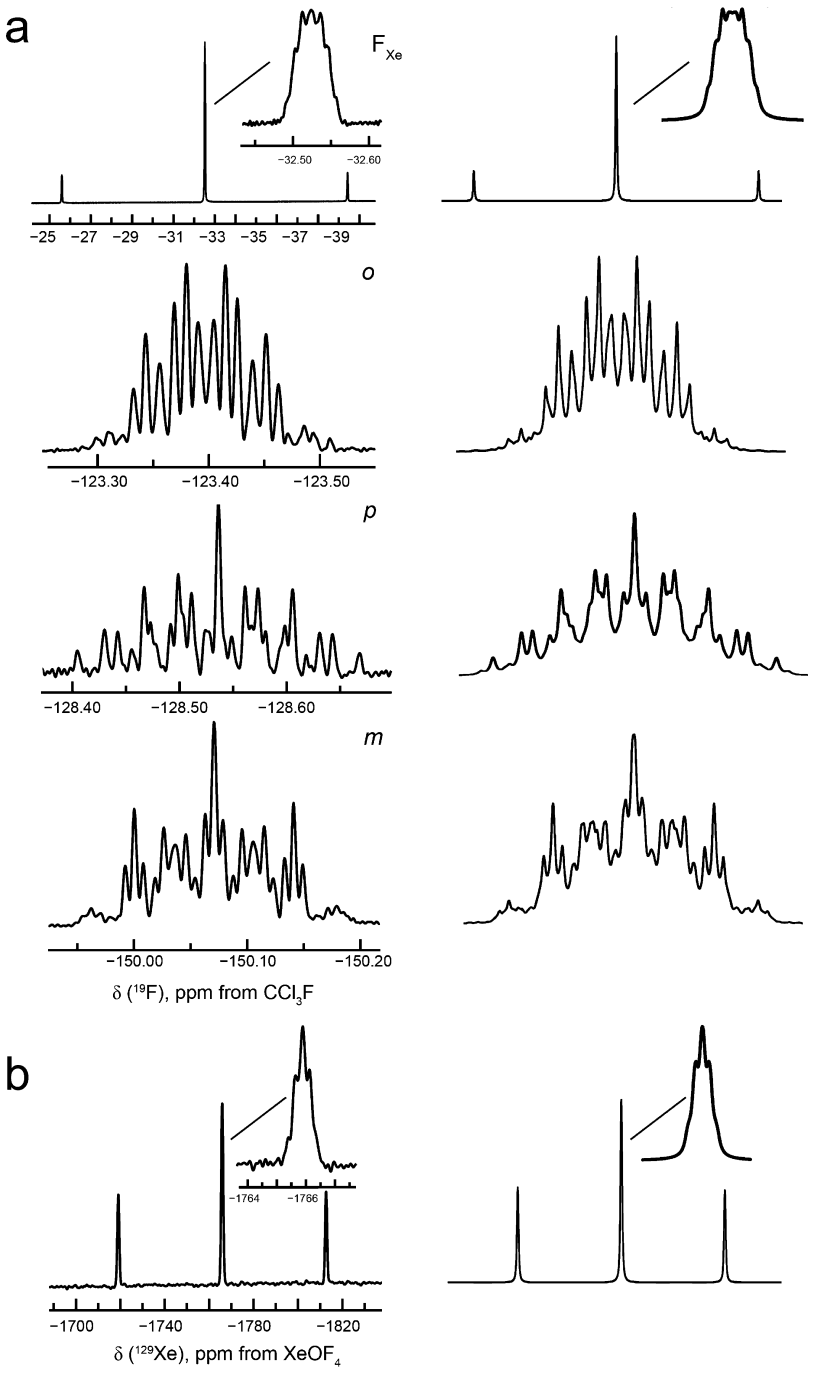

Figure 1. (a) The ^{19}F NMR spectrum (282.40 MHz) (F_{Xe}, *o*-, *p*-, *and m*-F) and (b) the ^{129}Xe NMR spectrum (83.02 MHz) of the $[C_6F_5XeF_2]^+$ cation in $[C_6F_5XeF_2][BF_4]$ (aHF, −40 °C). The experimental spectra, resolution-enhanced by Gaussian multiplication (left), and the simulated spectra (right) are shown.

cation to $[C_6F_5Xe]^+$ in the presence of $[C_6F_5BF_3]^-$ is attributable to fluorination and cleavage of the B−C bond of $[C_6F_5BF_3]^-$ to give C_6F_6 and $[BF_4]^-$ and fluorine addition to the C_6F_5 group of $[C_6F_5BF_3]^-$ to give $[C_6F_7BF_3]^-$. The rate of $[C_6F_5XeF_2]^+$ consumption in CH_3CN at −40 °C was ca. 10 times faster when a suspension of $[C_6F_5BF_3]^-$ was present. For a more detailed discussion of this topic, see Supporting Information.

(b) Reactivity of $[C_6F_5XeF_2][BF_4]$ with $Pn(C_6F_5)_3$ (Pn = P, As, or Bi) and C_6F_5X (X = Br or I). A preliminary communication provided a report of the fluorination of $P(C_6F_5)_3$, C_6F_5I, and I_2 to $P(C_6F_5)_3F_2$, $C_6F_5IF_2$, and IF_5 by $[C_6F_5XeF_2][BF_4]$ in CH_3CN.[38] The reactivities of $[C_6F_5XeF_2][BF_4]$ with $Pn(C_6F_5)_3$ (Pn = P, As, or Bi) and C_6F_5X in both CH_3CN and aHF were studied in the present work.

The triarylpnictogens, $Pn(C_6F_5)_3$ (Pn = P, As, or Bi), were fluorinated to $Pn(C_6F_5)_3F_2$ by $[C_6F_5XeF_2][BF_4]$ in CH_3CN at −40 °C over a period of 15 min, but no reaction occurred in aHF. The iodine atom of C_6F_5I was oxidatively fluorinated to $C_6F_5IF_2$ by $[C_6F_5XeF_2][BF_4]$ in CH_3CN and aHF (−40 °C within 15 min), but C_6F_5Br was unreactive under these conditions. Solutions of $[C_6F_5XeF_2][BF_4]$ in aHF at −20 °C also did not oxidize the bromine substituent but fluorinated the C_6F_5 group instead, providing a product mixture comprised of

dx.doi.org/10.1021/ic501831j | Inorg. Chem. XXXX, XXX, XXX−XXX

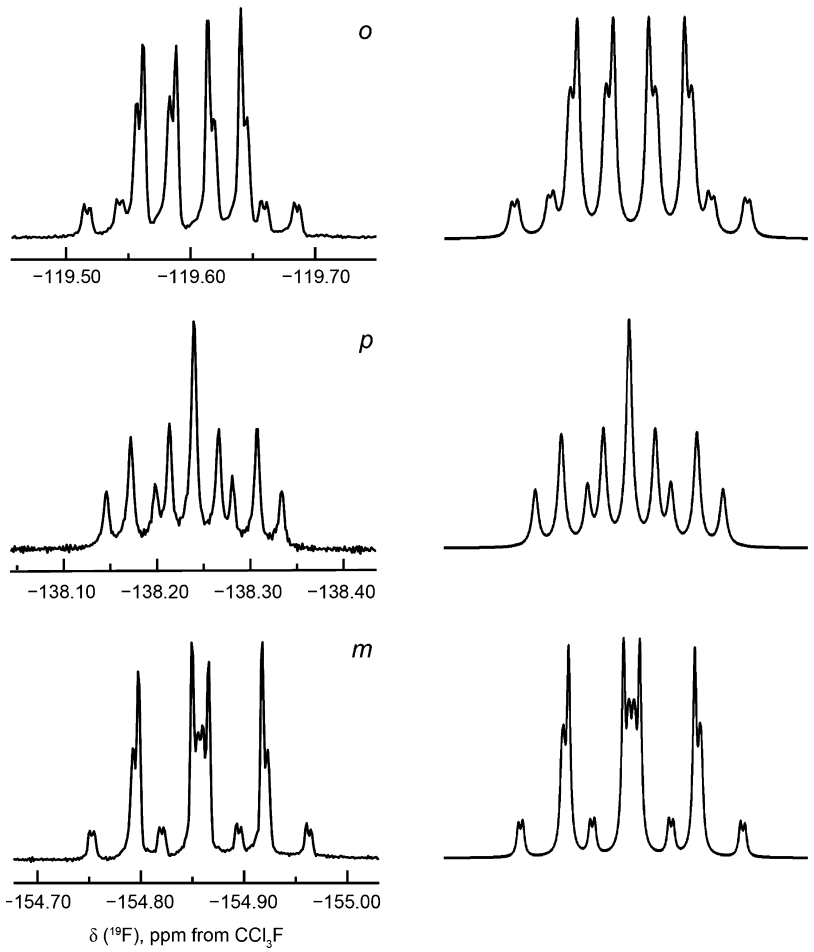

Figure 2. ^{19}F NMR spectra (282.40 MHz) of the *o-*, *p-*, *and m*-F ^{19}F environments in $C_6F_5IF_2$ (aHF, −80 °C). The experimental spectrum(left), resolution-enhanced by Gaussian multiplication (left), and the simulated spectrum (right) are shown.

Table 1. Coupling Constants (Hz) Derived from the Simulated ^{19}F NMR Spectra of $[C_6F_5XeF_2]^+$, $C_6F_5IF_2$, $[C_6F_5Xe]^+$, and C_6F_5I

	$[C_6F_5XeF_2]^{+a}$	$C_6F_5IF_2{}^b$	$[C_6F_5Xe]^{+c,d}$	$C_6F_5I^{d,e}$
$^1J(^{19}F_{Xe}-^{129}Xe)$	3902			
$^3J(^{19}F_o-^{129}Xe)$	19.05		67.7	
$^4J(^{19}F_m-^{129}Xe)$	21.61		8.8	
$^5J(^{19}F_p-^{129}Xe)$	8.23		3.7	
$^3J(^{19}F_o-^{19}F_m) = J_{23}$	−17.24	−20.64 [−22.65]	−20.2	−22.7
$^4J(^{19}F_o-^{19}F_p) = J_{24}$	10.38	7.33 [5.61]	8.24	2.1
$^5J(^{19}F_o-^{19}F_{m'}) = J_{25}$	−2.71	6.03 [6.30]	6.50	7.2
$^4J(^{19}F_o-^{19}F_{o'}) = J_{26}$	−17.01	−11.21 [−9.51]	−9.9	−4.9
$^3J(^{19}F_m-^{19}F_p) = J_{34}$	−19.39	−19.09 [−20.32]	−19.5	−19.5
$^4J(^{19}F_m-^{19}F_{m'}) = J_{35}$	2.50	0.85 [0.31]	0.83	−1.2
$^4J(^{19}F_{Xe}-^{19}F_o) = J_{12}$	3.27	3.16		
$^5J(^{19}F_{Xe}-^{19}F_m) = J_{13}$	2.30	−1.48		
$^6J(^{19}F_{Xe}-^{19}F_p) = J_{14}$	7.50	4.74		

[a]aHF (−40 °C). [b]aHF (−80 °C) [CH_2Cl_2 (24 °C)]. [c]CH_3CN (−40 °C). [d]Reference 40. [e]CD_3CN (24 °C).

$[C_6F_5XeF_2]^+$ (3), $[C_6F_5Xe]^+$ (9), C_6F_5Br (26), *c*-C_6F_7Br (8), *c*-C_6F_9Br (8), *c*-C_6F_8-1,4 (11), *c*-C_6F_{10} (1), C_6F_5Y (14) (where Y is unknown) C_6F_6 (21), and XeF_2 (6). The presence of $[C_6F_5Xe]^+$, C_6F_6, and *c*-C_6F_8-1,4 in the product mixture is consistent with the decomposition of the $[C_6F_5XeF_2]^+$ cation. For a more detailed discussion of this topic, see Supporting Information (Electrophilic Fluorination Properties of $[C_6F_5XeF_2][BF_4]$).

Characterization of $[C_6F_5XeF_2][BF_4]$ by ^{11}B, ^{13}C, ^{19}F, and ^{129}Xe NMR Spectroscopy. The ^{11}B, ^{13}C, ^{19}F, and ^{129}Xe NMR spectra of $[C_6F_5XeF_2][BF_4]$ (CH_3CN/CD_3CN, −40 °C) have been previously reported.[38] Only the chemical shifts, $^1J(^{19}F-^{129}Xe)$, and several $^1J(^{13}C-^{19}F)$ coupling constants were reported for $[C_6F_5XeF_2]^+$, but neither the $J(^{19}F-^{19}F)$ couplings nor the $J(^{19}F-^{129}Xe)$ couplings involving the C_6F_5 group could be resolved.[38] The present work provides a ^{11}B, ^{19}F, and ^{129}Xe

dx.doi.org/10.1021/ic501831j | Inorg. Chem. XXXX, XXX, XXX−XXX

NMR study of $[C_6F_5XeF_2][BF_4]$ in aHF solvent at −40 °C (Figure 1 and Supporting Information, Figure S1) and −80 °C (Supporting Information, Figure S2). The NMR parameters are listed in Supporting Information, Table S1 and a detailed discussion of the ^{19}F NMR spectrum of the $[BF_4]^-$ anion (−40 °C, aHF, Supporting Information, Figure S1) is provided. The ^{19}F NMR spectrum of isoelectronic $C_6F_5IF_2$ had also been previously reported in numerous solvents including CH_3CN (24 °C)[41] and aHF (−40 °C),[42] but the ^{19}F resonance of the IF_2 group could not be observed in aHF at −40 °C.[42] The present study also reports the ^{19}F NMR spectrum of $C_6F_5IF_2$ at −80 °C in aHF (Figure 2).

The ^{19}F NMR spectrum of $[C_6F_5XeF_2]^+$ in aHF is comprised of four multiplets (Figure 1a) having chemical shifts that are in good agreement with the published values.[38] The most deshielded ^{19}F environment is that of the XeF_2 group (−32.5 ppm, −40 °C and −33.2 ppm, −80 °C) which is a partially resolved multiplet flanked by satellite multiplets attributed to $^1J(^{19}F-^{129}Xe)$ (3902 Hz, −40 °C and 3889 Hz, −80 °C). The magnitude is in good agreement with that observed for $[C_6F_5XeF_2]^+$ in CH_3CN (3896 Hz, −40 °C) (Supporting Information, Table S1). In contrast, the fluorine resonance of the IF_2 group of $C_6F_5IF_2$ was not observed in aHF at −40 °C because its fluorine ligands are sufficiently fluoro-basic to undergo rapid ^{19}F chemical exchange with HF. The rate of ^{19}F chemical exchange was sufficiently slow in aHF at −80 °C to allow its observation as a broad singlet at −177.2 ppm ($\Delta\nu_{1/2}$ = 615 Hz). All $J(^{19}F-^{19}F)$ couplings involving the axial fluorine ligands of $C_6F_5IF_2$ were observed in CH_2Cl_2 (24 °C) (Table 1 and Supporting Information, Figure S3), but were absent in the spectra recorded in aHF (−40 and −80 °C) due to ^{19}F chemical exchange with HF solvent. The assignments of the $J(^{19}F-^{19}F)$ couplings involving the axial fluorine atoms of $C_6F_5IF_2$ (CH_2Cl_2, 24 °C) and $[C_6F_5XeF_2]^+$ (aHF, −40 °C) (Table 1) are confirmed by the excellent agreement between the experimental and simulated spectra (Figure S3, Supporting Information, and Figure 1, respectively). The absence of significant exchange broadening of the XeF_2 group resonance of $[C_6F_5XeF_2]^+$ at −40 °C in aHF is attributed to the lower ionic characters of the axial Xe−F bonds of $[C_6F_5XeF_2]^+$ relative to the I−F bonds of $C_6F_5IF_2$ (see Natural Bond Orbital (NBO) Analyses). Consequently, the fluorine atoms of the XeF_2 group are also considerably less shielded than those of the IF_2 group.

The *o*-, *m*-, and *p*-F environments of $[C_6F_5XeF_2]^+$ and $C_6F_5IF_2$ are more shielded in CH_3CN than in aHF (Supporting Information, Table S1). Their enhanced shieldings are attributed to CH_3CN coordination to Xe(IV)/I(III), which results in negative charge transfer to the aryl group (see Natural Bond Orbital (NBO) Analysis). Dissolution of $[C_6F_5XeF_2]^+$ and $C_6F_5IF_2$ in aHF may be promoted by hydrogen bonding with their basic Xe(IV)- and I(III)-bonded fluorine atoms, and may also contribute to their ^{19}F deshielding in aHF.

The ^{129}Xe NMR spectrum of $[C_6F_5XeF_2]^+$ (Figure 1; $\delta(^{129}Xe)$ = −1765.9 ppm, aHF, −40 °C) is a 1:2:1 triplet arising from $^1J(^{19}F-^{129}Xe)$ = 3902 Hz. The $^1J(^{19}F-^{129}Xe)$ coupling constant and ^{129}Xe chemical shift show little in the way of temperature or solvent dependencies in aHF ($\delta(^{129}Xe)$ = −1756.2 ppm, $^1J(^{19}F-^{129}Xe)$ = 3889 Hz, −80 °C) and CH_3CN ($\delta(^{129}Xe)$ = −1702.7 ppm, $^1J(^{19}F-^{129}Xe)$ = 3896 Hz, −40 °C) (Supporting Information, Table S1). Each branch of the triplet can be resolved into an overlapping triplet of triplets (Figure 1b, inset). The latter multiplet arises from similar ^{129}Xe couplings with F_o and F_m of the C_6F_5 group ($^3J(^{19}F_o-^{129}Xe) \approx {}^4J(^{19}F_m-^{129}Xe) \approx 20$ Hz), which appears as a pseudoquintet.

Complete sets of $J(^{19}F-^{19}F)$ and $J(^{19}F-^{129}Xe)$ couplings have now been obtained for the ^{19}F NMR spectra of $[C_6F_5XeF_2]^+$ (−40 °C, aHF), and complete sets of $J(^{19}F-^{19}F)$ couplings have also been obtained for $C_6F_5IF_2$ (−80 °C, aHF), which afforded the best-resolved spectra for simulation (Figures 1 and 2). The ^{19}F spectra were simulated using the multi-NMR simulation programs *gNMR*[43] and *ISOTOPOMER*.[44] The well-resolved multiplet fine structures observed for the F_p resonances of $[C_6F_5XeF_2]^+$ and $C_6F_5IF_2$, a triplet of triplets of triplets, provided preliminary values for $^3J(^{19}F_p-^{19}F_m)$, $^4J(^{19}F_p-^{19}F_o)$, and $^6J(^{19}F_p-^{19}F_{Xe})$. The F_o and F_m fluorine resonances exhibited partially resolved multiplet structures, which prevented direct extraction of the remaining $J(^{19}F-^{19}F)$ couplings. Moreover, the ^{129}Xe satellites ($I = {}^1/_2$, 26.44% natural abundance) associated with the ^{19}F resonances of the C_6F_5 group could not be fully resolved. Initial estimates of the missing $J(^{19}F-^{19}F)$ coupling constants were arrived at by using empirical relationships between the $^{19}F_p$ chemical shifts and their $^{19}F-^{19}F$ coupling constants as previously described for $[C_6F_5Xe]^+$ and C_6F_5I.[40] The observed chemical shifts and resulting estimated coupling constants were imported into *gNMR*, and the ^{19}F spectra of $[C_6F_5XeF_2]^+$ and $C_6F_5IF_2$ were simulated in manual and iterative modes. The couplings and their relative signs were then systematically varied to achieve the best fits with the experimental spectra. In the case of the $C_6F_5IF_2$ spectrum, which was better resolved than the $[C_6F_5XeF_2]^+$ spectrum, it proved possible to iterate the spectrum in the automatic iterative mode. The optimized coupling constants obtained from *gNMR*[43] were then imported, without further iteration, into the multi-NMR simulation program *ISOTOPOMER*,[44] which provided graphical representations that better reproduced all spectral features (Figures 1 and 2 and Supporting Information, Figure S3).

The signs of $^3J(^{19}F_o-^{19}F_m)$, $^3J(^{19}F_m-^{19}F_p)$, and $^4J(^{19}F_o-^{19}F_{o'})$ for $[C_6F_5XeF_2]^+$ are likely negative, and $^4J(^{19}F_o-^{19}F_p)$ is likely positive based on comparisons with $C_6F_5IF_2$, $[C_6F_5Xe]^+$, C_6F_5I (Table 1), and other C_6F_5-compounds.[45] The $^5J(^{19}F_o-^{19}F_{m'})$ coupling is assigned a negative sign because substitution of a positive sign greatly altered the appearance of the calculated spectrum. The remaining $J(^{19}F-^{19}F)$ ring couplings were either too small or lacked relevant literature values for comparison to confidently assign their relative signs. All trends in the relative magnitudes and signs of the *J*-values are in good agreement with those obtained from the spectral simulation of $C_6F_5IF_2$ (Table 1). Similar trends are observed when the $J(^{19}F-^{19}F)$ couplings of $[C_6F_5Xe^+]$ and C_6F_5I are compared (Table 1).[40,45]

X-ray Crystal Structures of $[C_6F_5XeF_2][BF_4]$ (1), $[C_6F_5XeF_2][BF_4]\cdot 2HF$ (2), and $[C_6F_5XeF_2][BF_4]\cdot 1.5CH_3CN$ (3a,b). A summary of the refinement results and other crystallographic information is provided in Table 2. Selected bond lengths and bond angles involving the xenon centers in $[C_6F_5XeF_2][BF_4]$ (Figure 3 and Supporting Information, Figure S4), $[C_6F_5XeF_2][BF_4]\cdot 2HF$ (Figure 4), and $[C_6F_5XeF_2][BF_4]\cdot 1.5CH_3CN$ (Figure 5) are listed in Table 3, and a full list of geometrical parameters that include the remaining geometrical parameters associated with xenon as well as the structural parameters of the $[BF_4]^-$ anions, C_6F_5 groups, and the coordinated CH_3CN and HF molecules are given in Supporting Information, Table S2. The latter parameters are in good agreement with previously published values[8,20,46−48] and do not require further comment.

dx.doi.org/10.1021/ic501831j | Inorg. Chem. XXXX, XXX, XXX−XXX

Table 2. Crystallographic Data for $[C_6F_5XeF_2][BF_4]$ (1), $[C_6F_5XeF_2][BF_4]\cdot 2HF$ (2), and $[C_6F_5XeF_2][BF_4]\cdot 1.5NCCH_3$ (3)

	1	2	3
chem formula	$C_6F_{11}BXe$	$C_6H_2F_{13}BXe$	$C_9H_{4.5}F_{11}BN_{1.5}Xe$
space group	$P2_1/n$	$P2_1/n$	$C2/c$
a (Å)	7.4707(2)	7.1022(2)	12.752(5)
b (Å)	19.0245(5)	19.5471(5)	23.520(5)
c (Å)	7.7595(2)	9.0812(2)	19.398(5)
β (deg)	109.873(1)	109.966(1)	103.213(5)
V (Å^3)	1037.15(5)	1184.94(5)	5664(3)
molecules/unit cell	4	4	4
mol wt (g mol^{-1})	423.17	463.19	1939.00
calcd density (g cm^{-3})	2.710	2.596	2.274
T (°C)	−173	−173	−173
μ (mm^{-1})	3.464	3.067	2.56
R_1[a]	0.0459	0.0417	0.0332
wR_2[b]	0.0887	0.0885	0.0897

[a] R_1 is defined as $\Sigma||F_0| - |F_c||/\Sigma|F_0|$ for $I > 2\sigma(I)$. [b] wR_2 is defined as $[\Sigma[w(F_0^2 - F_c^2)^2]/\Sigma w(F_0^2)^2]^{1/2}$ for $I > 2\sigma(I)$.

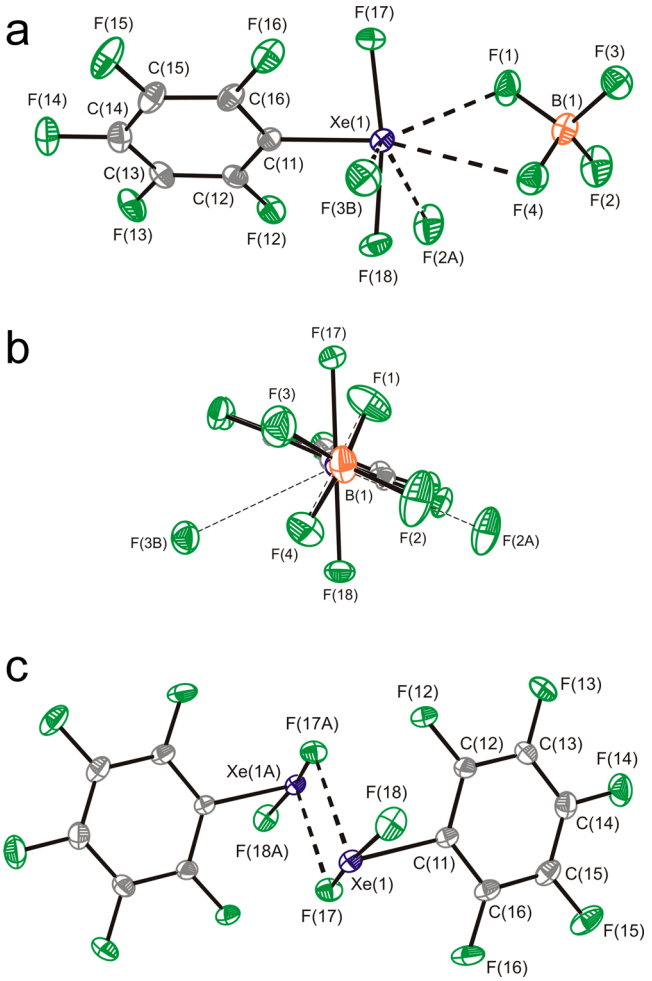

Figure 3. Structural unit in the crystal structure of $[C_6F_5XeF_2][BF_4]$ (a) showing the Xe---F_B cation−anion contacts. (b) A side-on view showing the Xe---F_B contacts and their avoidance of the trigonal plane containing C(11), Xe(1), and the two valence electron lone pairs of xenon. (c) A view showing the $[C_6F_5XeF_2]_2$ dimer units in $[C_6F_5XeF_2][BF_4]$. Thermal ellipsoids are shown at the 50% probability level.

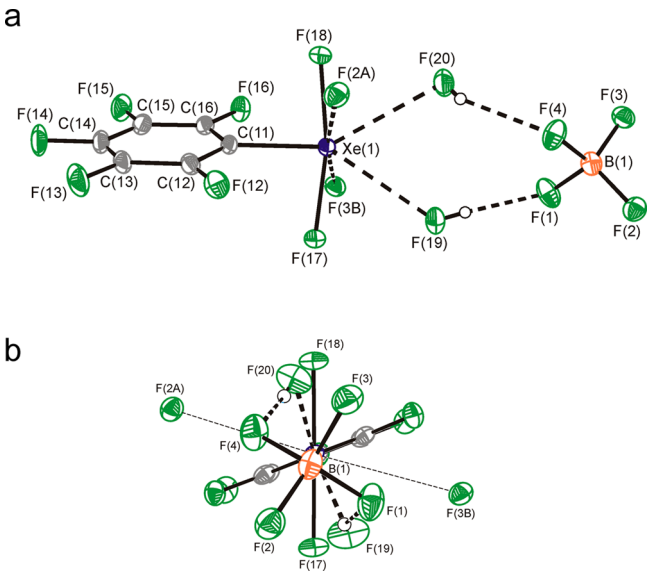

Figure 4. Structural unit in the crystal structure of $[C_6F_5XeF_2][BF_4]\cdot 2HF$ (a) showing the contacts, Xe---F(19,18)$_H$, F_B---H, and Xe---F_B. (b) A side-on view showing the Xe---F_H and Xe---F_B contacts viewed along the crystallographic b-axis and their avoidance of the trigonal plane containing C(11), Xe(1), and the two valence electron lone pairs of xenon. Thermal ellipsoids are shown at the 50% probability level.

The present study represents the only crystallographic characterization of Xe^{IV}−C bonds. The X-ray crystal structures of the isoelectronic $C_6F_5IF_2$ molecule[42] and its N-base adducts of 1,10-phenanthroline ($C_{12}H_8N_2$), 2,2′-bypyridine ($C_{10}H_8N_2$), and quinoline (C_9H_7N)[41] have been previously reported and are compared.

The Xe^{IV}−C bonds (**1**, 2.058(2); **2**, 2.058(3); **3a**, 2.067(4); **3b**, 2.066(5), 2.083(5) Å) are slightly shorter than the Xe^{II}−C bonds of $[C_6F_5Xe]^+$ salts (2.100(6)−2.104(5) Å)[46] and are not significantly affected by differences in contacts to xenon or by the higher positive charge on the Xe(IV) atom (see Natural Bond Orbital Analyses). The Xe−F bonds (**1**: 1.925(2), 1.948(2); **2**: 1.935(2), 1.941(2); **3a**: 1.930(2), 1.939(2); and **3b**: 1.940(2) Å) are significantly longer than the Xe−F_{ax} bonds of $[XeF_3]^+$ (1.894(2) and 1.901(2) Å in the $[SbF_6]^-$ salt;[48] 1.908(4) and 1.883(4) in the $[Sb_2F_{11}]^-$ salt[6]), but are only marginally shorter than the Xe−F bonds of XeF_4 (1.953(2) Å).[3] Electron transfer from the C_6F_5 group results in more polar Xe−F bonds than in the parent cations. The Xe−F bonds of $[C_6F_5XeF_2]^+$ are, in turn, significantly shorter and less polar than the I−F bonds of $C_6F_5IF_2$ (1.959(2)−2.025(2) Å) as a consequence of the higher positive charge and the electronegativity of Xe(IV).

The ligand arrangements around xenon and iodine in $[C_6F_5XeF_2]^+$ and $C_6F_5IF_2$[42] are T-shaped, in accordance with the AX_2YE_2 VSEPR arrangement of three bonding electron pairs and two electron lone pairs in the xenon/iodine valence shell. The more electronegative fluorine atoms occupy the axial positions, and the less electronegative C_6F_5 group and the two xenon/iodine valence electron lone pairs occupy the equatorial plane. In all three Xe(IV) crystal structures, the C(11), Xe(1), F(17), and F(18) atoms are coplanar within $\pm 3\sigma$. The electron lone pair domains cause the F−Xe(I)−F angles to bend toward the C_6F_5 group producing nonlinear F−Xe(I)−F angles (**1**, 170.22(7); **2**, 168.7(1); **3a**, 170.5(1); and **3b**, 165.5(2) and 167.3(1)°). Similar bent F−I−F angles are observed for

dx.doi.org/10.1021/ic501831j | Inorg. Chem. XXXX, XXX, XXX−XXX

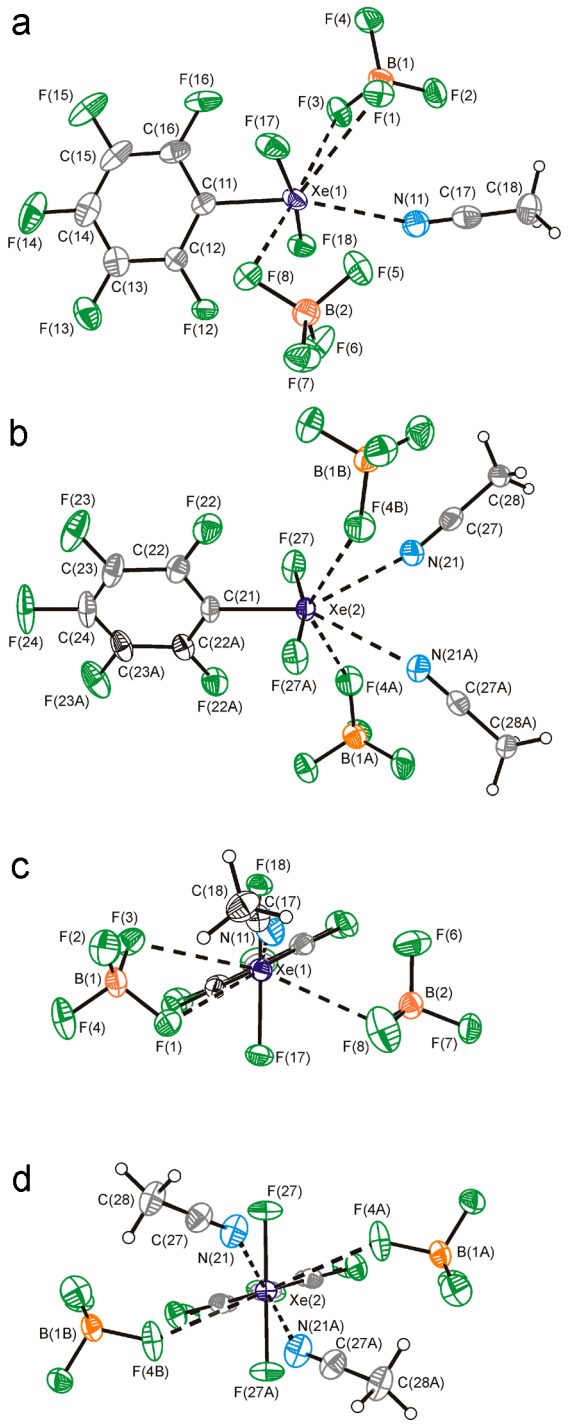

Figure 5. The two solvated cations in the crystal structure of $[C_6F_5XeF_2][BF_4]\cdot 1.5CH_3CN$: (a) $[C_6F_5XeF_2]\cdot CH_3CN$ solvate and its Xe---F_B contacts with two adjacent $[BF_4]^-$ anions and (b) one of two crystallographically nonequivalent $[C_6F_5XeF_2]\cdot 2CH_3CN$ solvates and its Xe---F_B contacts with two adjacent $[BF_4]^-$ anions. (c, d) The side-on views of the Xe---N and Xe---F_B contacts, shown along the crystallographic *b*-axes, depict their avoidance of the trigonal planes containing C(11/12), Xe(1/2) and the two valence electron lone pairs of xenon. Thermal ellipsoids are shown at the 50% probability level.

isoelectronic $C_6F_5IF_2$ and its nitrogen base adducts ($C_6F_5IF_2$: 170.46(10) and 171.59(9)°;[42] $C_6F_5IF_2$ adducts: 161.07(7) ($C_{12}H_8N_2$),[41] 158.63(8) ($C_{10}H_8N_2$),[41] 165.86(8) and 172.59(8)° (C_9H_7N)[41]). The XeF_2 moieties are twisted out of the plane orthogonal to the C_6F_5 plane in the crystal structures of $[C_6F_5XeF_2]^+$, with F–Xe–C_{ipso}–$C^{2,6}$ dihedral angles of **1**, 67.5(2); **2**, 68.3(3); **3a**, 62.5(3); **3b**, 75.2(2), and 79.4(2)°. The calculated geometries of $[C_6F_5XeF_2][BF_4]$, $[C_6F_5XeF_2][BF_4]\cdot 2HF$, $[C_6F_5XeF_2]^+\cdot CH_3CN$, and $[C_6F_5XeF_2]^+\cdot 2CH_3CN$ show that the Xe---F and Xe---N contacts significantly influence the above angles (see Computational Results). Comparable dihedral angles occur for the two crystallographically distinct $C_6F_5IF_2$ molecules in the crystallographic unit cell of $C_6F_5IF_2$ (74.40(3), 74.7(3)°)[42] and the N-base adducts of $C_6F_5IF_2$ (59.0(2), 59.1(2)° ($C_{12}H_8N_2$); 68.9(2), 71.5(2)°, ($C_{10}H_8N_2$); 63.8(3), 68.3(3)° (C_9H_7N)).[41]

The xenon atom of $[C_6F_5XeF_2][BF_4]$ shows two short contacts, Xe(1)---F(1), 2.686(2) Å and Xe(1)---F(4), 2.833(2) Å, with two fluorine atoms of the same $[BF_4]^-$ anion. The Xe---F contacts are significantly less than the sum of the van der Waals radii of Xe and F (3.63 Å)[49] and are significantly shorter than the Xe---F contact in $[C_6F_5Xe][B(CF_3)_4]$ (2.913(4) Å),[46] indicating that the $[BF_4]^-$ anion is more strongly coordinated to the $[C_6F_5XeF_2]^+$ cation than $[B(CF_3)_4]^-$ is to the $[C_6F_5Xe]^+$ cation, which is consistent with the greater anticipated Lewis acidity of $[C_6F_5XeF_2]^+$ and lower fluorobasicity of $[B(CF_3)_4]^-$. Unfortunately, the structural parameters of $[C_6F_5Xe][BF_4]$ cannot be compared because its crystal structure has not been determined. As expected, the B–F_B bonds, where the F_B atoms are involved in Xe---F_B contacts (B(1)–F(1), 1.406(3) Å and B(1)–F(4), 1.407(4) Å), are slightly elongated relative to the terminal B–F bonds (B(1)–F(2), 1.369(3) Å and B(1)–F(3), 1.386(4) Å). When the coordination sphere is enlarged to 3.5 Å, two additional long contacts with two different $[BF_4]^-$ anions, Xe(1)---F(2A) and Xe(1)---F(3B), are found at 2.937(2) and 3.073(2) Å, respectively. As depicted in Figure 3, the Xe---F_B contacts avoid the trigonal plane containing C(11), Xe(1) and the two valence electron lone pairs of xenon. The two shorter contacts approach from above and below the trigonal plane, whereas the two longer contacts approach from below the trigonal plane. These fluorine contacts approach xenon from opposite sides of the Xe(1),C(11),F(17),F(18)-plane, which is orthogonal to the trigonal plane. A third, long intermolecular Xe(1)---F_{Xe} contact (3.137(2) Å) occurs with a second $[C_6F_5XeF_2]^+$ cation in $[C_6F_5XeF_2][BF_4]$ (Figure 3). The long contacts result in weakly bonded four-membered $(XeF)_2$ dimer rings between adjacent $[C_6F_5XeF_2]^+$ cations, which pack along the *c*-axis (Supporting Information, Figure S4). The $[C_6F_5XeF_2]^+$ dimers form zigzag chains along the *b*-axis that are separated by alternating layers of $[BF_4]^-$ anions (Supporting Information, Figure S4). The $(XeF)_2$ rings are similar to the $(IF)_2$ rings found in the X-ray crystal structures of $C_6F_5IF_2$[42] and $C_6F_5IF_2\cdot C_9H_7N$.[41] Unlike the $(XeF)_2$ rings of $[C_6F_5XeF_2][BF_4]$, the $(IF)_2$ rings of $C_6F_5IF_2$ are part of an infinite chain structure. The smallest angle around Xe is the cation–anion contact angle F(1)---Xe(1)---F(4) (47.90(5)°), which is constrained by the near-tetrahedral F(1)–B(1)–F(4) angle as well as by the Xe(1)---F(1,4) contact distances.

The xenon atom of $[C_6F_5XeF_2][BF_4]\cdot 2HF$ shows two short contacts, Xe(1)---F(19) (2.855(2) Å) and Xe(1)---F(20) (2.800(3) Å), with the fluorine atoms of two crystallographically distinct HF molecules. The Xe---F contacts are significantly shorter than the sum of the van der Waals radii of Xe and F (3.63 Å)[49] and are comparable to the Xe---F contacts observed in $[C_6F_5XeF_2][BF_4]$ (vide supra).[46] Each HF molecule interacts with two fluorine atoms of the same $[BF_4]^-$ anion (F(19)---F(1), 2.543(4) Å and F(20)---F(4),

dx.doi.org/10.1021/ic501831j | Inorg. Chem. XXXX, XXX, XXX–XXX

Table 3. Selected Experimental Geometrical Parameters of $[C_6F_5XeF_2][BF_4]$, $[C_6F_5XeF_2][BF_4]\cdot 2HF$, and $[C_6F_5XeF_2][BF_4]\cdot 1.5NCCH_3$[a]

$[C_6F_5XeF_2][BF_4]$		$[C_6F_5XeF_2][BF_4]\cdot 2HF$		$[C_6F_5XeF_2][BF_4]\cdot 1.5NCCH_3$			
Bond Lengths (Å)[b]							
Xe(1)-C(11)	2.058(2)	Xe(1)-C(11)	2.058(3)	Xe(1)-C(11)	2.067(4)	Xe(2)-C(21)	2.083(5)
Xe(1)-F(17)	1.948(2)	Xe(1)-F(17)	1.941(2)			Xe(3)-C(31)	2.066(5)
				Xe(1)-F(17)	1.939(2)	Xe(2)-F(27)	1.940(2)
Xe(1)-F(18)	1.925(2)	Xe(1)-F(18)	1.935(2)	Xe(1)-F(18)	1.930(2)	Xe(3)-F(37)	1.940(2)
Xe(1)---F(1)	2.686(2)	Xe(1)---F(19)	2.855(2)	Xe(1)---N(11)	2.742(4)	Xe(2)---N(21)	2.816(4)
Xe(1)---F(4)	2.833(2)	Xe(1)---F(20)	2.800(3)			Xe(3)---N(31)	2.868(4)
				Xe(1)---F(1)	2.959(3)	Xe(2)---F(4)	3.028(3)
Xe(1)---F(2A)	2.937(2)	Xe(1)---F(2A)	3.040(3)	Xe(1)---F(3)	3.041(3)	Xe(3)---F7)	3.036(3)
Xe(1)---F(3B)	3.073(2)	Xe(1)---F(3B)	3.110(3)	Xe(1)---F(8)	3.049(3)		
				N(11)-C(17)	1.146(6)	N(21)-C(27)	1.149(6)
Xe(1)---F(17A)	3.137(2)					N(31)-C(37)	1.135(6)
		F(1)---F(19)	2.543(4)	C(17)-C(18)	1.406(6)	C(27)-C(28)	1.423(6)
		F(4)---F(20)	2.550(4)			C(37)-C(38)	1.463(7)
Bond Angles (deg)[b]							
C(11)-Xe(1)-F(17)	83.97(8)	C(11)-Xe(1)-F(17)	84.0(1)	C(11)-Xe(1)-F(17)	86.1(1)	C(21)-Xe(2)-F(27)	82.75(8)
C(11)-Xe(1)-F(18)	86.27(8)	C(11)-Xe(1)-F(18)	84.7(1)			C(31)-Xe(3)-F(37)	83.65(7)
C(11)-Xe(1)---F(1)	153.10(7)	C(11)-Xe(1)---F(19)	145.1(1)	C(11)-Xe(1)-F(18)	84.5(1)	C(21)-Xe(2)-F(27A)	82.75(8)
C(11)-Xe(1)---F(4)	158.30(7)	C(11)-Xe(1)---F(20)	149.5(1)			C(31)-Xe(3)-F(37A)	83.65(7)
C(11)-Xe(1)---F(2A)	111.89(7)	C(11)-Xe(1)---F(2A)	94.8(1)	C(11)-Xe(1)---N(11)	159.4(1)	C(21)-Xe(2)---N(21)	148.20(8)
C(11)-Xe(1)---F(3B)	80.44(7)	C(11)-Xe(1)---F(3B)	92.3(1)			C(21)-Xe(2)---N(21A)	148.20(8)
						C(31)-Xe(3)---N(31)	147.71(8)
						C(31)-Xe(3)---N(31A)	147.71(8)
F(17)-Xe(1)-F(18)	170.22(7)	F(17)-Xe(1)-F(18)	168.7(1)	F(17)-Xe(1)-F(18)	170.5(1)	F(27)-Xe(2)-F(27A)	165.5(2)
						F(37)-Xe(3)-F(37A)	167.3(1)
F(17)-Xe(1)---F(4)	112.51(7)	F(17)-Xe(1)---F(20)	125.2(1)	F(17)-Xe(1)---N(11)	114.2(1)	F(27)-Xe(2)---N(21A)	124.9(1)
F(17)-Xe(1)---F(2A)	114.83(7)	F(17)-Xe(1)---F(2A)	107.5(1)			F(27A)-Xe(2)---N(21)	124.9(1)
F(17)-Xe(1)---F(3B)	112.91(6)	F(17)-Xe(1)---F(3B)	75.4(1)			F(37)-Xe(3)---N(31A)	69.6(1)
F(18)-Xe(1)---F(1)	118.67(7)	F(18)-Xe(1)---F(19)	127.0(1)			F(37A)-Xe(3)---N(31)	69.6(1)
F(17)-Xe(1)---F(1)	70.82(7)	F(17)-Xe(1)---F(19)	64.1(1)	F(18)-Xe(1)---N(11)	75.3(1)	F(27)-Xe(2)---N(21)	69.1(1)
F(18)-Xe(1)---F(4)	77.11(7)	F(18)-Xe(1)---F(20)	65.9(1)			F(27A)-Xe(2)---N(21A)	69.1(1)
F(18)-Xe(1)---F(2A)	68.43(8)	F(18)-Xe(1)---F(2A)	72.9(1)			F(37)-Xe(3)---N(31)	122.4(1)
F(18)-Xe(1)---F(3B)	65.90(7)	F(18)-Xe(1)---F(3B)	105.6(1)			F(37A)-Xe(3)---N(31A)	122.4(1)
F(1)---Xe(1)---F(4)	47.90(5)	F(19)---Xe(1)---F(20)	65.29(9)			N(21)---Xe(2)---N(21A)	63.6(1)
F(1)---Xe(1)---F(2A)	72.42(7)	F(19)---Xe(1)---F(2A)	107.57(9)			N(31)-Xe(3)---N(31A)	64.6(1)
Dihedral Angles (deg)[b]							
F(17)-Xe(1)-C(11)-C(12)	67.5(2)	F(17)-Xe(1)-C(11)-C(12)	68.3(3)	F(17)-Xe(1)-C(11)-C(12)	62.5(3)	F(27)-Xe(1)-C(21)-C(22)	75.2(2)
						F(37)-Xe(3)-C(31)-C(32)	79.4(2)

[a]The labeling schemes correspond to those used in Figures 3, 4, and 5, respectively. [b]A full list of geometrical parameters is given in Supporting Information, Table S2.

2.550(4) Å). As observed for $[C_6F_5XeF_2][BF_4]$, the B−F_B bonds, where the F_B ligands are hydrogen-bonded to HF or coordinated to xenon, are elongated (Figure 4). When the xenon coordination sphere is enlarged to 3.5 Å, two additional long contacts with two different $[BF_4]^-$ anions, Xe(1)---F(2A) and Xe(1)---F(3B), are found at 3.040(3) and 3.110(3) Å, respectively. The Xe---F contacts avoid the trigonal plane containing C(11), Xe(1), and the two valence electron lone pairs of xenon and are directed away from the C_6F_5 group in a manner similar to that observed in $[C_6F_5XeF_2][BF_4]$. The local geometry around the xenon atom is similar to that observed in the $[C_6F_5XeF_2][BF_4]$ ion pair except for the F(17)−Xe(1)---F(19) (64.1(1)°) and F(18)−Xe(1)---F(20) (65.9(1)°) angles, which are more closed, and the F(19)---Xe(1)---F(20) angle, which is more open (65.29(9)°).

The crystal structure of $[C_6F_5XeF_2][BF_4]\cdot 1.5CH_3CN$ contains three types of solvates, two crystallographically nonequivalent $[C_6F_5XeF_2][BF_4]\cdot 2CH_3CN$ and one $[C_6F_5XeF_2][BF_4]\cdot CH_3CN$ salt formulations (Figure 5). The asymmetric units of $[C_6F_5XeF_2][BF_4]\cdot 2CH_3CN$ are on C_2-axes, whereas the $[C_6F_5XeF_2][BF_4]\cdot CH_3CN$ structural unit is on a general position, giving rise to the same number of $[C_6F_5XeF_2][BF_4]\cdot 2CH_3CN$ and $[C_6F_5XeF_2][BF_4]\cdot CH_3CN$ units in the unit cell and the average formulation $[C_6F_5XeF_2][BF_4]\cdot 1.5CH_3CN$.

The xenon atom coordination spheres in $[C_6F_5XeF_2][BF_4]\cdot 1.5CH_3CN$ are comprised of contacts with CH_3CN and $[BF_4]^-$, which are geometrically similar to those of $[C_6F_5XeF_2][BF_4]$ and $[C_6F_5XeF_2][BF_4]\cdot 2HF$. The $[C_6F_5XeF_2]^+$ cation of $[C_6F_5XeF_2][BF_4]\cdot 2CH_3CN$ has two Xe---N contacts with two symmetry-related CH_3CN molecules in which the CH_3CN geometries are not noticeably affected by coordination. The Xe---N contact distances, 2.816(4) and 2.868(4) Å, are comparable to the Xe---F contact distances in $[C_6F_5XeF_2][BF_4]$ and $[C_6F_5XeF_2][BF_4]\cdot 2HF$, but are longer than the Xe---N contact distances in $[C_6F_5Xe]^+\cdot CH_3CN$ (2.613(15) and 2.637(7) Å).[46] The angles subtended at the xenon atoms are similar to those of $[C_6F_5XeF_2][BF_4]$ except for the N---Xe---N angles (63.6(1) and 64.6(1)°), which are comparable to the corresponding F---Xe---F angle in $[C_6F_5XeF_2][BF_4]\cdot 2HF$ (65.29(9)°). The $[C_6F_5XeF_2]^+$ cation of the $[C_6F_5XeF_2][BF_4]\cdot CH_3CN$ unit has one Xe---N contact with the CH_3CN molecule (2.742(4) Å). The next shortest contacts are Xe---F contacts with the fluorine atoms of the $[BF_4]^-$ anions (**3a**: 2.959(3), 3.041(3), and 3.049(3) Å; **3b**: 2 × 3.028(3) and 2 × 3.036(3) Å), which are comparable to those in $[C_6F_5XeF_2][BF_4]$ and $[C_6F_5XeF_2][BF_4]\cdot 2HF$. Again, the Xe---F contacts avoid the trigonal plane containing C(11), Xe(1), and the two valence electron lone pairs of xenon (Figures 3 and 4). The C−Xe---N angles of $[C_6F_5XeF_2]^+\cdot 2CH_3CN$ (148.20(8)° and 147.71(8)°) and $[C_6F_5XeF_2]^+\cdot CH_3CN$ (159.4(1)°) deviate more from linearity than the C−Xe---N and C−Xe---F angles in $[C_6F_5Xe][B(CF_3)_4]$ (174.8(2)°),[46] $[C_6F_5Xe\cdot CH_3CN][B(C_6F_5)_2F_2]\cdot CH_3CN$ (174.5(3)°),[50] $[C_6F_5Xe\cdot CH_3CN][B(C_6F_5)_4]$ (177.1 (4)°),[46] and C_6F_5Xe---$NCB(CN)_3$ (175.9(1)°).[46]

Raman Spectroscopy. The low-temperature, solid-state Raman spectra of the $[C_6F_5XeF_2][BF_4]$ (**1**) ion pair and the

dx.doi.org/10.1021/ic501831j | Inorg. Chem. XXXX, XXX, XXX−XXX

$[C_6F_5XeF_2][BF_4]$·2HF (**2**) HF-solvated ion pair (Figures 6 and 7 and Supporting Information, Figures S5 and S6) were

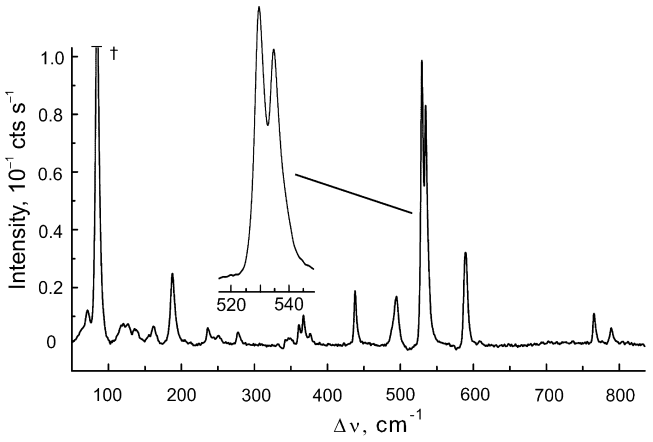

Figure 6. Raman spectrum of $[C_6F_5XeF_2][BF_4]$ recorded in a Pyrex glass NMR tube at −155 °C using 1064-nm excitation. The symbol (†) denotes an instrumental artifact. Bands that occur in the 835–1835 cm^{-1} region of the spectrum are given in Table 4 and are shown in Supporting Information, Figure S5.

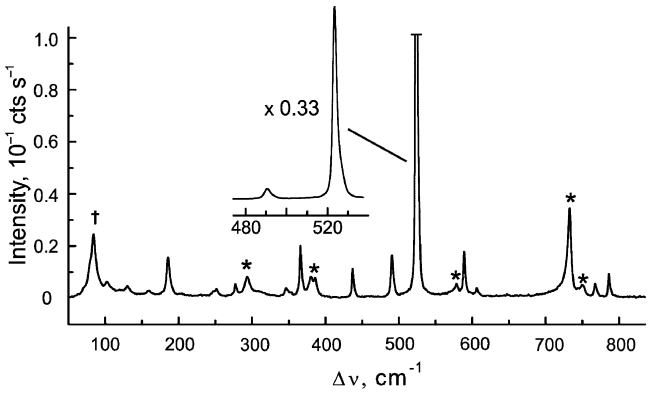

Figure 7. Raman spectrum of $[C_6F_5XeF_2][BF_4]$·2HF recorded in a FEP sample tube at −155 °C using 1064-nm excitation. The symbols denote bands arising from an instrumental artifact (†) and the FEP sample tube (*). Bands that occur in the 835–1835 cm^{-1} region of the spectrum are listed in Table 4 and are shown in Supporting Information, Figure S6.

assigned under C_1 symmetry based on their experimental and calculated geometries and are provided in Table 4. A total of 51 (**1**) and 63 (**2**) Raman- and infrared-active bands are predicted. The frequency assignments were aided by the calculated frequencies and Raman intensities of $[C_6F_5XeF_2][BF_4]$ and $[C_6F_5XeF_2][BF_4]$·2HF and by previous vibrational assignments for $[C_6F_5Xe]^+$,[46] the C_6F_5 group,[51−55] and $[BF_4]^-$.[56] The calculations were carried out using the B3LYP and PBE1PBE (values given in square brackets) functionals and aug-cc-pVTZ(-PP) basis sets. The experimental Raman and infrared frequencies of $C_6F_5IF_2$ have been reported, but were not assigned.[42] Complete assignments of the Raman and infrared spectra of $C_6F_5IF_2$ are provided in the ensuing discussion, allowing a comparison of the vibrational frequencies of $C_6F_5IF_2$ with those of the isoelectronic $[C_6F_5XeF_2]^+$ cation (Table 5). Overall, there is good agreement between the calculated and observed frequencies of both species.

The majority of the vibrational frequencies and their descriptions for the C_6F_5 groups of $[C_6F_5XeF_2][BF_4]$, $[C_6F_5XeF_2][BF_4]$·2HF, and $C_6F_5IF_2$ are very similar to those of $[C_6F_5Xe]^+$,[46] C_6F_5I,[53−55] and related C_6F_5 derivatives,[51,52] and therefore do not require further commentary.

Factor-group analyses[57] of (**1**) and (**2**) were carried out by correlating their calculated gas-phase geometries (C_1) to their crystal site symmetries (C_1) and, in turn, to their unit cell symmetries (C_{2h}) (Supporting Information, Tables S3 and S4). The analyses reveal that vibrational coupling within the crystallographic unit cell leads to splitting of each vibrational band of (**1**) into four components, two Raman-active A_g and B_g components, and two infrared-active A_u and B_u components. In the experimental spectra (Table 4), many of the Raman bands of (**1**) are split, but no band splittings were resolved for (**2**), indicating that vibrational coupling within the unit cell of (**2**) is weak.

(a) $[C_6F_5XeF_2][BF_4]$ (1) and $[C_6F_5XeF_2][BF_4]$·2HF (2). The bands at 789 (**1**) and 786 (**2**) cm^{-1} are assigned to the extensively coupled ν(Xe(1)−C(1)) − [ν(C(3)−C(4)) + ν(C(5)−C(4))] − [ν(C(3)−F(3)) + ν(C(5)−F(5))] mode. The experimental frequencies are in good agreement with the calculated values ((**1**), 788 [811]; (**2**), 787 [812] cm^{-1}; Table 4) and are in accordance with the observed Xe−C_{ipso}, $C^{3,5}$−C^4, and $C^{3,5}$−$F^{3,5}$ bond lengths, which are equal in both salts (Table 3). This mode is shifted to higher frequency relative to that of the isolated $[C_6F_5XeF_2]^+$ cation. The calculations show that the Xe−C stretch also contributes to a low-frequency mode, which is strongly coupled to the $\delta(XeF_2)_{i.p}$ deformation mode ((**1**), 251 [260] cm^{-1}; (**2**), 245 [271] cm^{-1}). The $\delta(XeF_2)_{i.p.}$ mode is also coupled to ν(Xe---F_B) of (**1**) (197 [203] cm^{-1}) and ν(Xe---F_H) of (**2**) (190 [195] cm^{-1}). As predicted, the majority of these low-frequency modes correspond to weak to very weak bands in the Raman spectra ((**1**), 213 and 188 cm^{-1}; (**2**), 248 and 186 cm^{-1}), except for the band at 188 cm^{-1}, which has medium intensity. The contribution of ν(Xe−C) to both a high- and a low-frequency mode has also been observed for the $[C_6F_5Xe]^+$ cation.[46]

The $\nu_s(XeF_2)$ bands of $[C_6F_5XeF_2]^+$ in (**1**) and (**2**) are calculated at 507 [536] and 524 [551] cm^{-1}, respectively, and correspond to the most intense Raman bands in their experimental Raman spectra (530/535 (**1**) and 524 (**2**) cm^{-1}). The splittings in the Raman spectrum of $[C_6F_5XeF_2]$-$[BF_4]$ (**1**) arise from vibrational coupling within the crystallographic unit cell (vide supra, Supporting Information, Table S3). The calculated $\nu_{as}(XeF_2)$ frequencies are 565 [589] cm^{-1} (**1**) and 587 [609] cm^{-1} (**2**) and are predicted to be very weak because of the near-centrosymmetric local geometry of the XeF_2 group. Consequently, these modes were observed in the experimental Raman spectra as very weak bands (608/609 (**1**) and 606 (**2**) cm^{-1}). Both frequencies are comparable to $\nu_{as}(XeF_{2ax})$ (619 cm^{-1}) and $\nu_s(XeF_{2ax})$ (583 cm^{-1}) in $[XeF_3][Sb_2F_{11}]$,[58] but occur at higher frequencies relative to XeF_4, i.e., $\nu_{as}(XeF_4)$ (solid, 502 cm^{-1};[59] gas, 524 cm^{-1}[60]) and $\nu_s(XeF_4)$ (solid, 543 cm^{-1};[59] gas: 554 cm^{-1}[60]). The calculated frequencies of the $\nu_s(XeF_2)$ and $\nu_{as}(XeF_2)$ modes of $[C_6F_5XeF_2][BF_4]$·2HF (**2**) (ν_s, 524 [551] cm^{-1}; ν_{as}, 587 [609] cm^{-1}) are in good agreement with those predicted for gas-phase $[C_6F_5XeF_2]^+$ (ν_s, 524 [556] cm^{-1}; ν_{as}, 600 [634] cm^{-1}), but are shifted to lower frequencies in (**1**) (ν_s, 507 [536] cm^{-1}; ν_{as}, 565 [589] cm^{-1}). In contrast with the $\delta(XeF_2)_{i.p.}$ deformation modes of (**1**) and (**2**), which were shown to be coupled to ν(Xe−C) (vide supra), the out-of-

dx.doi.org/10.1021/ic501831j | Inorg. Chem. XXXX, XXX, XXX−XXX

Table 4. Experimental Raman Frequencies and Intensities for $[C_6F_5XeF_2][BF_4]$ and $[C_6F_5XeF_2][BF_4]\cdot 2HF$ and Calculated Vibrational Frequencies, Intensities, and Assignments for $[C_6F_5XeF_2][BF_4]$ and $[C_6F_5XeF_2][BF_4]\cdot 2HF$

$[C_6F_5XeF_2][BF_4]$			$[C_6F_5XeF_2][BF_4]\cdot 2HF$			
exptl[a,b,c]	B3LYP[d]	PBE1PBE[d]	exptl[a,c,e]	B3LYP[d]	PBE1PBE[d]	assgnts (C_1)[f]
			2590(<1), br	2876(389)[4472][g]	2804(474)[6489][g]	ν_s(HF)
				2627(237)[2136]	2677(66)[420]	ν_{as}(HF)
1634, sh	1655(5)[<1]	1691(4)[<1]	1630(5)	1652(4)[<1]	1693(4)[<1]	ν(C–C)
1629(11)	1635(21)[24]	1673(17)[26]	1616(<1)	1633(25)[25]	1672(18)[24]	
1521(4)	1534(<1)[430]	1574(<1)[452]	1527(2)	1537(1)[438]	1579(<1)[452]	ν(C–C) / ν(C–F)
1519, sh	1528(6)[286]	1568(6)[300]		1529(7)[322]	1570(5)[330]	
1513(4)						
1440(2)	1430(<1)[30]	1468(<1)[20]	1442(<1)	1431(<1)[34]	1472(<1)[22]	
1442(2)			1429(2)			
1431(4)						
1427(5)						
	1304(3)[16]	1340(2)[16]	1297(2)	1306(2)[16]	1343(2)[21]	ν(C–C)
			1282(<1)			
	1303(2)[4]	1334(1)[5]		1305(1)[8]	1337(<1)[4]	ν(C–C) / ν(C–F)
1180(3)	1178(2)[2]	1213(2)[3]	1178(1)	1184(3)[2]	1219(2)[2]	
	1104(11)[130]	1132(10)[123]	1113(<1)	1107(10)[112]	1136(8)[118]	
	1008(<1)[184]	1032(<1)[173]		1012(<1)[175]	1037(<1)[160]	
				1111(3)[191]	1147(1)[188]	F–H---F_B deformation modes
				997(4)[154]	1064(4)[258]	
				989(9)[127]	1020(5)[125]	
				967(<1)[22]	982(2)[54]	
	1267(2)[352]	1292(1)[350]		1267(1)[425]	1290(<1)[403]	$\nu_{as}(BF_2)$
	1082(2)[856]	1108(2)[852]	1045(<1)	1054(8)[687]	1078(7)[640]	
	820(17)[212]	851(12)[217]		825(3)[246]	837(1)[201]	
	763(<0.1)[0]	772(<0.1)[<0.1]		763(<1)[<1]	774(<0.1)[<1]	$\delta(CCC)_{i.p.}$
789(5)	788(7)[26]	811(6)[20]	786(3)	787(5)[31]	812(4)[31]	ν(Xe–C) / ν(C–C) / ν(C–F)[g]
	750(<0.1)[<1]	759(<0.1)[1]	647(<1)	749(<0.1)[<1]	757(<0.1)[<1]	$\delta(CCC)_{o.o.p.}$
	676(<0.1)[0]	685(<0.1)[<0.1]		676(<0.1)[<0.1]	684(<0.1)[<0.1]	
765(12)	732(4)[113]	746(5)[101]	767(2)	735(10)[157]	747(9)[168]	$\nu_s(BF_2)$
609(1)	565(<1)[132]	589(<1)[141]	606(1)	587(<1)[161]	609(<1)[169]	$\nu_{as}(XeF_2)$
608(2)						
	639(<1)[1]	649(<1)[<1]		637(<1)[2]	645(<1)[1]	$\delta(CCC)_{o.o.p.}$
589(33)	589(10)[2]	596(11)[2]	589(6)	590(9)[3]	598(10)[3]	$\delta(CCC)_{i.p.}$
	539(3)[33]	546(17)[31]		501(<1)[3]	509(<1)[<1]	$\delta(BF_2)_{out\ of\ phase}$
535(84)	507(98)[<1]	536(62)[9]	523(100)	524(87)[<1]	551(69)[<1]	$\nu_s(XeF_2)$
530(100)						
495(18)	495(14)[<0.1]	501(16)[<1]	491(5)	495(18)[<0.1]	501(16)[2]	$\delta(CCC)_{i.p.}$
438(18)	442(4)[<0.1]	442(4)[<0.1]	437(4)	441(4)[<0.1]	442(4)[<1]	
423(1)						
	492(<0.1)[7]	497(<0.1)[7]		526(3)[22]	504(2)[16]	$\rho_w(BF_2)$ / $\rho_t(BF_2)$
	492(<1)[5]	501(<1)[5]		530(<1)[16]	549(1)[8]	
				416(<1)[11]	459(<1)[22]	F–H---(BF_4) deformation modes
376(3)	387(1)[3]	398(1)[4]		382(<1)[1]	388(<1)[4]	$\delta(CCC)_{o.o.p.}$
	369(2)[0]	379(2)[0]		364(2)[<0.1]	374(2)[<0.1]	
367(10)	385(<1)[67]	390(<1)[69]	366(6)	385(<1)[12]	368(<1)[12]	$\delta(BF_2)_{in\ phase}$
361(6)						
353(1)	347(5)[<1]	353(4)[<1]	353, sh	348(5)[1]	354(5)[2]	$\delta(CCF)_{i.p.}$
349(2)			346(1)			
347(2)						
343(1)						
	309(<0.1)[1]	311(<0.1)[1]		310(<0.1)[1]	313(<0.1)[1]	
278(4)	278(<0.1)[<0.1]	277(<0.1)[<0.1]	277(1)	280(1)[4]	282(2)[46]	
	278(1)[5]	279(2)[16]		279(<0.1)[<0.1]	276(<0.1)[<0.1]	
	321(<1)[0]	325(<1)[0]		315(<1)[4]	305(<1)[5]	$\rho_t(BF_2)$
				290(<1)[6]	322(<1)[3]	$\rho_t(BF_2)$ / ν(Xe---F_H)$_{in\ phase}$
236(6)	241(1)[2]	247(1)[1]	252(1)	238(1)[9]	251(<1)[7]	$\delta(CCF)_{o.o.p.}$ / $\rho_t(XeF_2)$
213(1)	251(<1)[118]	260(<1)[109]	248(<1)	245(1)[107]	271(<1)[81]	$\delta(XeF_2)_{i.p.}$ / ν(Xe–C)
205(2)	216(<0.1)[11]	224(<0.1)[11]		232(<1)[24]	239(<1)[5]	$\delta(XeF_2)_{o.o.p.}$
203(2)						
188(25)	197(2)[43]	203(3)[46]	186(5)	190(8)[57]	195(9)[68]	ν(Xe---$F_{H/B}$)$_{out\ of\ phase}$ / $\delta(XeF_2)_{i.p.}$
	182(<1)[<1][x]	186(<1)[<1]		178(<1)[1]	188(<1)[2]	$\delta(CCF)_{o.o.p.}$ / $\rho_t(XeF_2)$
			160(<1)	166(4)[13]	175(2)[19]	δ(F---Xe---F)$_{i.p.}$
162(5)	165(0)[1]	176(<0.1)[2]				$\rho_t(XeF_2) + \rho_t(BF_2) - \delta(CCF)_{o.o.p.}$
156(2)	152(<1)[2]	156(<1)[1]		148(<1)[<1]	162(<1)[<1]	$\rho_t(XeF_2)$ / $\delta(CCF)_{o.o.p.}$
				134(<1)[2]	147(<1)[2]	deformation mode
138(4)	135(9)[25]	140(6)[27]				
136(4)						
127(6)	133(<0.1)[0]	133(<0.1)[0]	130(1)	133(<0.1)[<0.1]	137(<0.1)[<0.1]	$\delta(CCF)_{o.o.p.}$
			102(2)	115(2)[4]	115(1)[<1]	deformation mode
121(6)	125(<1)[<1]	127(<1)[<1]				$\delta(CCXe)_{i.p.}$ / $\delta(XeF_2)_{o.o.p.}$
118(5)				109(<1)[7]	106(<1)[<1]	deformation mode
	102(<1)[<0.1]	105(<1)[<1]				$\rho_t(XeF_2) - \rho_t(BF_2) + \delta(CCF)_{o.o.p.}$
				95(<1)[5]	95(<1)[11]	deformation modes
				85(2)[4]	81(<1)[2]	
				75(<1)[<1]	79(2)[4]	
				53(1)[<1]	56(<1)[6]	
	51(<1)[<1]	51(<1)[<1]		40(<1)[3]	49(<1)[<1]	
	39(<1)[0]	43(<1)[0]		30(<0.1)[<0.1]	30(<1)[<1]	
	37(<1)[2]	37(<1)[1]		23(<1)[<1]	24(<1)[<1]	
	17(<0.1)[1]	16(<0.1)[1]		16(<1)[<1]	16(<0.1)[<1]	
	13(2)[0]	6(2)[0]		4(<1)[1]	13(<1)[1]	

[a]Frequencies are given in cm^{-1}. The abbreviations denote a shoulder (sh) and broad (br). [b]The Raman spectrum was recorded at −150 °C in 4-mm o.d. Pyrex glass sample tube. [c]Values in parentheses denote relative Raman intensities. [d]The aug-cc-pVTZ(-PP) basis set was used. Values in parentheses denote calculated Raman intensities ($Å^4$ amu^{-1}), and values in square brackets denote calculated infrared intensities (km mol^{-1}). [e]The Raman spectrum was recorded at −150 °C in a $^1/_4$-in. o.d. FEP sample tube. [f]The deformation modes of the C_6F_5 ring are denoted by δ and are

dx.doi.org/10.1021/ic501831j | Inorg. Chem. XXXX, XXX, XXX–XXX

Table 4. continued

relative to the plane of the C_6F_5 ring; i.p. and o.o.p. denote in-plane and out-of-plane, respectively. The deformation modes of the XeF_2 group are relative to a plane passing through the XeF_2 group and the C(1) atom, i.e., $\delta(XeF_2)_{i.p.}$ denotes a bend within the $CXeF_2$ plane, and $\delta(XeF_2)_{o.o.p.}$ denotes bending out of this plane. The symbols ν, ρ_r, and ρ_t denote a stretch, a rock, and a twist. [g]The detailed description is $\nu(Xe(1)-C(1)) - [\nu(C(3)-C(4)) + \nu(C(5)-C(4))] - [\nu(C(3)-F(3)) + \nu(C(5)-F(5))]$.

Table 5. Experimental Vibrational Frequencies and Intensities for $[C_6F_5XeF_2]^+$ in $[C_6F_5XeF_2][BF_4]$ and for $C_6F_5IF_2$, and Calculated Vibrational Frequencies, Intensities, and Assignments for $[C_6F_5XeF_2]^+$ and $C_6F_5IF_2$

$[C_6F_5XeF_2]^+$			$C_6F_5IF_2$				$[C_6F_5XF_2]^{+/0}$ (X = Xe or I)
exptl[a,b]	B3LYP[c]	PBE1PBE[c]	exptl[a,d]	exptl[a,e]	B3LYP[c]	PBE1PBE[c]	assgnts (C_1)[f]
1634, sh 1629(11)	1637(<1)[<1] 1613(30)[29]	1675(<1)[<1] 1654(23)[26]	1636(10)	1637, m	1647(3)[<1] 1646(13)[34]	1685(3)[<1] 1681(13)[34]	ν(C–C)
1521(4) 1519, sh 1513(4)	1545(<1)[459] 1529(39)[402]	1586(<1)[480] 1570(32)[414]	1512(3)	1521, vs	1518(<1)[432] 1528(4)[238]	1559(<1)[453] 1567(4)[255]	
1440(2) 1442(2) 1431(4) 1427(5)	1425(16)[11]	1460(15)[7]	1408(3)	1409, m	1423(8)[14]	1463(9)[8]	ν(C–C) / ν(C–F)
	1311(1)[37]	1349(<1)[38]		1376, m 1346, m	1302(1)[7]	1338(<1)[9]	ν(C–C)
	1307(14)[6]	1340(10)[7]		1296, m	1299(<1)[7]	1329(<1)[7]	
1180(3)	1198(3)[1]	1232(2)[2]	1153(3)	1154, m	1166(2)[3]	1202(2)[3]	
	1111(<1)[114]	1139(<1)[116]	1090(2)	1100, s	1105(3)[137]	1133(2)[137]	ν(C–C) / ν(C–F)
	1021(<1)[159]	1043(<1)[150]		1047, w 1013, m 989, vs	1001(<1)[194]	1026(<1)[181]	
	764(<0.1)[<0.1]	773(<0.1)[<0.1]			759(<1)[<0.1]	768(<1)[<1]	$\delta(CCC)_{i.p.}$
789(5)	755(17)[26]	782(12)[20]	812(3)	813, s	808(1)[35]	829(1)[32]	ν(X–C) / ν(C–C) / ν(C–F)[g]
	746(<0.1)[<0.1]	754(<0.1)[1]		722, m	752(<0.1)[<1]	759(<0.1)[1]	$\delta(CCC)_{o.o.p.}$
	672(<0.1)[0]	681(<0.1)[<0.1]			680(<0.1)[<0.1]	688(<0.1)[<0.1]	
609(1) 608(2)	600(5)[116]	634(<1)[139]		547, sh 541, s	529(<1)[237]	551(<1)[240]	$\nu_{as}(XF_2)$[h]
	616(<1)[54]	621(4)[42]	625(1)	625, m	649(<1)[2]	655(<1)[2]	$\delta(CCC)_{o.o.p.}$[i]
589(33)	590(10)[2]	597(10)[3]	586(22)	585, w	589(11)[<1]	596(12)[<1]	$\delta(CCC)_{i.p.}$
535(84) 530(100)	524(105)[24]	556(85)[22]	533(100)	532, s	509(37)[5]	532(31)[4]	$\nu_s(XF_2)$
495(18)	491(9)[3]	497(9)[1]	496(29) 478(2)	487, sh 479, s 472, s	497(10)[<1]	503(11)[<1]	$\delta(CCC)_{i.p.}$
438(18) 423(1)	434(4)[<1]	435(4)[<1]	441(49)	446, s 437, s	445(4)[<0.1]	446(4)[<1]	
376(3)	347(<0.1)[3] 333(2)[0]	364(<0.1)[4] 350(2)[0]	386(21)	393, s 387, s	389(1)[3] 380(2)[<0.1]	394(1)[4] 388(3)[<0.1]	$\delta(CCC)_{o.o.p.}$
353(1) 349(2) 347(2) 343(1)	342(<1)[<1]	349(<1)[<1]	354(10)	352, m	354(2)[<0.1]	359(2)[<0.1]	$\delta(CCF)_{i.p.}$
	308(<0.1)[2]	311(<0.1)[2]			312(<0.1)[1]	314(<0.1)[1]	
278(4)	278(<0.1)[<0.1] 277(<1)[<1]	276(<0.1)[<0.1] 277(<1)[1]	281(5)		279(<0.1)[<0.1] 282(<1)[<1]	278(<0.1)[<0.1] 281(<1)[2]	
236(6)	231(1)[2]	238(1)[2]			232(<1)[2]	236(<1)[1]	$\delta(CCF)_{o.o.p.}$ / $\rho_r(XF_2)_{small}$
213(1)	208(<1)[43]	220(<1)[47]	241(10)		224(1)[38]	230(<1)[39]	ν(X–C) / $\delta(XF_2)_{i.p.}$
205(2) 203(2)	207(<0.1)[11]	215(<0.1)[11]			200(<0.1)[14]	205(<0.1)[13]	$\delta(XF_2)_{o.o.p.}$
162(5) 156(2)	172(<1)[<1]	175(<1)[<1]			175(<0.1)[<1]	178(<0.1)[<1]	$\delta(CCF)_{o.o.p.}$ / $\rho_r(XF_2)_{small}$
188(25)	160(5)[4]	168(5)[3]	174(25)		158(3)[10]	165(3)[9]	$\delta(XF_2)_{i.p.}$
127(6)	131(<0.1)[<1] 130(<1)[<1]	132(<0.1)[0] 132(<1)[<1]	150(4) 130(8)		132(<0.1)[<0.1] 132(<1)[<1]	133(<0.1)[<0.1] 139(<1)[<1]	$\delta(CCF)_{o.o.p.}$ $\rho_r(XF_2)$ / $\delta(CCF)_{o.o.p.}$
121(6) 118(5)	117(<1)[<1]	119(<1)[<1]	96(47)		124(<1)[<0.1]	120(<1)[<0.1]	$\rho_r(CCF)_{i.p.}$ / $\delta(CCX)_{i.p.}$
	54(2)[<1]	56(2)[<0.1]			57(2)[<0.1]	58(2)[<0.1]	$\rho_r(XF_2) + \rho_t(CCF)_{o.o.p.}$
	25(3)[0]	25(3)[0]			12(2)[<0.1]	19(2)[<0.1]	$\rho_t(XF_2) + \rho_t(CCF)_{o.o.p.}$

[a]Frequencies are given in cm^{-1}. The abbreviation denotes a shoulder (sh). [b]The Raman spectrum was recorded at −150 °C in a $^1/_4$-in. o.d. FEP sample tube. Values in parentheses denote relative Raman intensities. Bands at 765(10), 367(10), 361(6), and 353(1) cm^{-1} were assigned to $[BF_4]^-$ by comparison with previous assignments given in ref 56 and by comparison with the assignments reported for $[C_6F_5XeF_2][BF_4]$ in Table 4. [c]The aug-cc-pVTZ(-PP) basis set was used. Values in parentheses denote calculated Raman intensities ($Å^4$ amu^{-1}), and values in square brackets denote calculated infrared intensities (km mol^{-1}). [d]Raman frequencies and relative Raman intensities are from ref 42. [e]Infrared frequencies and intensities are from ref 42. The abbreviations denote weak (w), medium (m), strong (s), and very strong (vs). [f]The C_6F_5 ring deformation modes are denoted by δ and are relative to the plane containing the C_6F_5 ring; i.p. and o.o.p. denote in-plane and out-of-plane, respectively. The deformation modes of the XF_2 group are described relative to a plane passing through the XF_2 group and the C(1) atom, i.e., $\delta(XF_2)_{i.p.}$ denotes a bend within the CXF_2 plane, and $\delta(XF_2)_{o.o.p.}$ denotes bending out of this plane. The symbols ν, ρ_r, and ρ_t denote a stretch, a rock, and a twist. [g]The detailed description is $\nu(X(1)-C(1)) - [\nu(C(3)-C(4)) + \nu(C(5)-C(4))] - [\nu(C(3)-F(3)) + \nu(C(5)-F(5))]$. [h]In the xenon case, there is also a small contribution from $\delta(CCC)_{o.o.p.}$ at both levels of theory. [i]In the xenon case, there is also a small contribution from $\nu_{as}(XeF_2)$ at both levels of theory.

plane counterparts, $\delta(XeF_2)_{o.o.p.}$, are not significantly coupled to any other modes. The $\delta(XeF_2)_{o.o.p.}$ modes are predicted to occur as very weak Raman bands at 216 [224] (**1**) and 232 [239] cm^{-1} (**2**), respectively, and correspond to weak bands at 203 and 205 cm^{-1} in the experimental spectrum of $[C_6F_5XeF_2][BF_4]$. In contrast, the $\rho_r(XeF_2)$ deformation modes are predicted to couple with $\delta(CCF)_{o.o.p.}$ to give three weak Raman bands at 152, 182, 241 [156, 186, 247] cm^{-1} (**1**) and 148, 178, 238 [162, 188, 251] cm^{-1} (**2**); however, only two weak bands were observed for (**1**) (156 and 236 cm^{-1}), and

dx.doi.org/10.1021/ic501831j | Inorg. Chem. XXXX, XXX, XXX–XXX

Table 6. Selected Calculated[a] Geometrical Parameters for $[C_6F_5XeF_2][BF_4]$, $[C_6F_5XeF_2][BF_4]\cdot 2HF$, $[C_6F_5XeF_2]^+\cdot 2NCCH_3$, $[C_6F_5XeF_2]^+$, and $C_6F_5IF_2$

	$[C_6F_5XeF_2][BF_4]$ (C_1)[b]		$[C_6F_5XeF_2][BF_4]\cdot 2HF$ (C_1)[b]		$C_6F_5XeF_2^+\cdot 2NCCH_3$ (C_1)[b]		$C_6F_5XeF_2^+$ (C_{2v})[b]		$C_6F_5IF_2$ (C_2)[b]	
					Bond Lengths (Å)					
X = Xe, I	B3LYP	PBE1PBE	B3LYP	PBE1PBE	B3LYP	PBE1PBE	B3LYP	PBE1PBE	B3LYP	PBE1PBE
X(1)-C(1)	2.116	2.085	2.102	2.078	2.106	2.073	2.090	2.056	2.090	2.067
X(1)-F(11)	1.982	1.957	1.969	1.947	1.978	1.953	1.963	1.938	2.009	1.986
X(1)-F(12)	1.982	1.957	1.978	1.948	1.978	1.953	1.963	1.938	2.009	1.986
Xe(1)---F(13)	2.481	2.451								
Xe(1)---F(14)	2.481	2.452								
Xe(1)---F(17)			2.558	2.556						
Xe(1)---F(18)			2.605	2.538						
F(13)---F(17)			2.364	2.357						
F(14)---F(18)			2.390	2.350						
Xe(1)---N(1)					2.795	2.764				
Xe(1)---N(2)					2.795	2.764				
					Bond Angles (deg)					
F(11)-X(1)-F(12)	161.8	161.7	166.6	164.2	164.5	165.1	178.3	177.8	172.2	171.3
F(11)-X(1)-C(1)	80.9	80.8	83.2	82.1	82.3	82.5	89.2	88.9	86.1	85.7
F(12)-X(1)-C(1)	80.9	80.8	83.4	82.2	82.3	82.5	89.2	88.9	86.1	85.7
F(11)-Xe(1)---F(13)	72.1	71.9								
F(11)-Xe(1)---F(14)	126.2	126.4								
F(12)-Xe(1)---F(13)	126.2	126.4								
F(12)-Xe(1)---F(14)	72.1	71.9								
F(11)-Xe(1)---F(17)			118.0	124.3						
F(11)-Xe(1)---F(18)			71.8	70.4						
F(12)-Xe(1)---F(17)			74.0	70.1						
F(12)-Xe(1)---F(18)			120.0	124.1						
F(13)---Xe(1)---F(14)	54.1	54.6								
C(1)-Xe(1)---F(13)	152.9	152.7								
C(1)-Xe(1)---F(14)	152.9	152.7								
F(17)---Xe(1)---F(18)			69.7	70.4						
C(1)-Xe(1)---F(17)			145.5	144.5						
C(1)-Xe(1)---F(18)			144.7	145.0						
Xe(1)---F(13)-B(1)	102.8	102.5								
Xe(1)---F(14)-B(1)	102.8	102.5								
F(11)-Xe(1)---N(1)					68.2	68.7				
F(11)-Xe(1)---N(2)					126.6	125.5				
F(12)-Xe(1)---N(1)					126.6	125.5				
F(12)-Xe(1)---N(2)					68.2	68.7				
N(1)---Xe(1)---N(2)					66.4	66.7				
C(1)-Xe(1)---N(1)					146.8	146.7				
C(1)-Xe(1)---N(2)					146.8	146.7				
Xe(1)---N(1)-C(7)					169.1	169.9				
Xe(1)---N(2)-C(9)					169.0	169.9				
					Dihedral Angles (deg)					
F(11)-X(1)-C(1)-C(2)	90.0	90.0	79.6	65.5	88.6	82.3	90.0	90.0	92.8	103.9
F(12)-X(1)-C(1)-C(2)	–90.0	–90.0	–100.7	–114.5	–91.4	–97.7	–90.0	–90.0	–87.2	–76.1

[a]The aug-cc-pVTZ(-PP) basis set was used. [b]The labeling schemes correspond to those used in Figure 8.

only one weak band was observed for (**2**) (252 cm^{-1}). A broad band at 2590 cm^{-1} (not shown in Supporting Information, Figure S6) was assigned to the HF stretching bands (Table 4).

(b) $C_6F_5IF_2$ and Its Comparison with $[C_6F_5XeF_2]^+$. The Raman band at 812 cm^{-1} is assigned to the coupled mode, $\nu(I(1)-C(1)) - [\nu(C(3)-C(4)) + \nu(C(5)-C(4))] - [\nu(C(3)-F(3)) + \nu(C(5)-F(5))]$ (Table 5). The experimental frequency shifts 23/26 cm^{-1} to higher frequency when going from $[C_6F_5XeF_2][BF_4]$ (789 cm^{-1}) and $[C_6F_5XeF_2][BF_4]\cdot 2HF$ (786 cm^{-1}) to $C_6F_5IF_2$ (812 cm^{-1}) and by 20/21 [18/17] cm^{-1} for their calculated values (Xe, 788/787 [811/812]; I, 808 [829] cm^{-1}). A similar pattern was found for the corresponding stretching modes of $[C_6F_5Xe][BF_4]$ and C_6F_5I (experimental: Xe, 795 and I, 808 cm^{-1}; calculated: Xe, 760 [782] and I, 807 [826] cm^{-1}).[46] The I–C stretching mode of $C_6F_5IF_2$ also contributes to a low-frequency mode (224 [230]), and is strongly coupled to the $\delta(IF_2)_{i.p.}$ deformation mode. This mode appears as a medium-intensity band at 241 cm^{-1}. The Xe^{IV}–C and I^{III}–C stretching frequencies of $[C_6F_5XeF_2]^+$ and $[C_6F_5IF_2]$ occur at higher frequencies than the Xe^{II}–C and I^{I}–C stretching frequencies of $[C_6F_5Xe]^+$ and C_6F_5I owing to the greater electronegativities of I(III) and Xe(IV) and consequent greater covalent characters of their I^{III}–C and Xe^{IV}–C bonds. The $\nu_s(IF_2)$ frequency of $C_6F_5IF_2$ is calculated to be only 20 [19] cm^{-1} lower than that of $\nu_{as}(IF_2)$. Both values are intermediate with respect to the corresponding calculated frequencies of $[C_6F_5XeF_2]^+$, which differ by 76 [78] cm^{-1}. The symmetric IF_2 stretch of $C_6F_5IF_2$ (533 cm^{-1}) was observed as the most intense band in its Raman spectrum.[42] The asymmetric stretch, $\nu_{as}(IF_2)$, was not observed in the Raman spectrum in contrast with $[C_6F_5XeF_2]^+$ where it was observed as a weak, split band (vide supra); however, $\nu_{as}(IF_2)$ was observed as a very intense band in the infrared spectrum (541 cm^{-1}).[42] The corresponding $\nu_s(IF_{2ax})$ and $\nu_{as}(IF_{2ax})$ modes of IF_3 occur at similar frequencies (488[61] and 480[62] cm^{-1}, respectively), but the frequency order is reversed in $C_6F_5IF_2$. The $\delta(IF_2)_{o.o.p.}$ deformation mode is predicted to occur as a very weak Raman band at 200 [205] cm^{-1}, but was not observed. In contrast, and as noted above, the $\delta(IF_2)_{i.p.}$ deformation mode is coupled to $\nu(I-C)$. For comparison, the $\delta(IF_{2ax})$ mode of IF_3 occurs at 217 cm^{-1}.[61]

Computational Results. The electronic structures of $[C_6F_5XeF_2][BF_4]$, $[C_6F_5XeF_2][BF_4]\cdot 2HF$, $[C_6F_5XeF_2]^+$, $C_6F_5IF_2$, and $[C_6F_5XeF_2]^+\cdot 2CH_3CN$ were calculated using the

dx.doi.org/10.1021/ic501831j | Inorg. Chem. XXXX, XXX, XXX–XXX

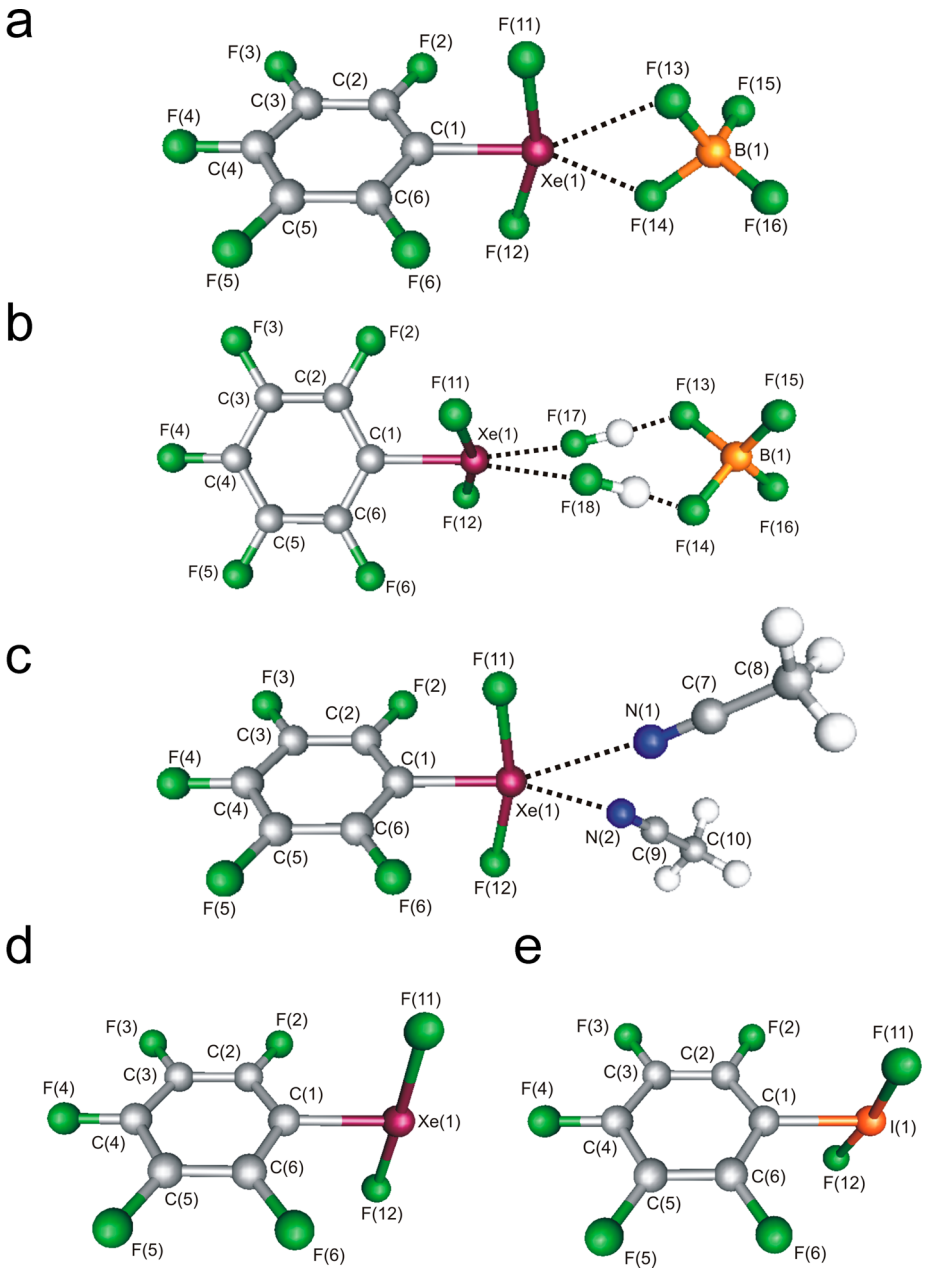

Figure 8. Energy-minimized gas-phase geometries of (a) $[C_6F_5XeF_2][BF_4]$, (b) $[C_6F_5XeF_2][BF_4]\cdot 2HF$, (c) $[C_6F_5XeF_2]^+\cdot 2NCCH_3$, (d) $[C_6F_5XeF_2]^+$, and (e) $C_6F_5IF_2$ (B3LYP/aug-cc-pVTZ(-PP)).

B3LYP and PBE1PBE (values given in square brackets) functionals and the aug-cc-pVTZ(-PP) basis sets starting from the crystallographic coordinates (C_1 symmetry). The gas-phase structure of $[C_6F_5XeF_2]^+\cdot CH_3CN$ was also calculated to study the effect of coordinating a single CH_3CN ligand to $[C_6F_5XeF_2]^+$. All calculations resulted in stationary points with all frequencies real. The electronic structures of C_6F_5I, $C_6F_5IF_2$, $[C_6F_5Xe]^+$, $[C_6F_5Xe]^+\cdot CH_3CN$, C_6F_6, $[XeF_3]^+$, IF_3, $[XeF]^+$, IF, $[BF_4]^-$, HF, and CH_3CN were also calculated at the same levels of theory to allow comparisons of their respective charges, valencies, and bond orders. Molecular orbitals and NBO analyses for all species were carried out with NBO 6.0[63] at the same levels of theory. The electronic structure of $C_6F_5IF_2$ was calculated to compare its geometrical and vibrational frequencies with those of $[C_6F_5XeF_2]^+$. The basis sets employed semirelativistic effective core potentials (RLC ECP); consequently, the present calculated values for $C_6F_5IF_2$ were improved when compared with the previously reported values obtained at the RHF/LANL2DZ level.[42] Calculated vibrational frequencies, intensities, and geometrical parameters are reported in Tables 4−6 and Supporting Information, Tables S5−S12, and energy-minimized structures are shown in Figure 8 and Supporting Information, Figures S7 and S8.

(a) Geometries. The calculated geometrical parameters of the C_6F_5 rings in $[C_6F_5XeF_2]^+$ and $C_6F_5IF_2$ are in good agreement with the experimental values and remain essentially unchanged upon coordination of $[C_6F_5XeF_2]^+$ to HF or CH_3CN and ion pairing with $[BF_4]^-$. Therefore, these geometric parameters are not further commented on in the ensuing discussion but are listed in Supporting Information, Table S5.

dx.doi.org/10.1021/ic501831j | Inorg. Chem. XXXX, XXX, XXX−XXX

(i) $[C_6F_5XeF_2][BF_4]$ (1) and $[C_6F_5XeF_2][BF_4]\cdot 2HF$ (2). The calculations reveal that both the ion pair (**1**) and the HF-solvated ion pair (**2**) are stable entities whose solid-state geometries are well-reproduced by the gas-phase calculations. As observed experimentally, the calculated Xe−C (2.116 [2.085] Å) and Xe−F (1.982 [1.957] Å) bond lengths of (**1**) are in good agreement with those of (**2**) (Xe−C, 2.102 [2.078] Å; Xe−F, 1.969 [1.947] and 1.978 [1.948] Å). When compared with their experimental values ((**1**): Xe−C, 2.058(2) Å; Xe−F, 1.925(2) and 1.948(2) Å; (**2**): Xe−C, 2.058(3) Å; Xe−F, 1.935(2) and 1.941(2) Å), the calculated Xe−C and Xe−F bond lengths are slightly elongated for (**1**) and (**2**). The Xe---F_B bond lengths of (**1**) (2.481 [2.451] and 2.481 [2.452] Å) and the Xe---F_H (2.558 [2.556] and 2.605 [2.538] Å), and the F_B---F_H (2.364 [2.357] and 2.390 [2.350] Å) bond lengths of (**2**) are underestimated compared to their experimental values ((**1**): Xe---F_B, 2.686(2) and 2.833(2) Å; (**2**): Xe---F_H, 2.800(3) and 2.855(2) Å, F_B---F_H, 2.543(4) and 2.550(4) Å). As expected, upon ion pairing or coordination to HF, the two B−F_B bonds of the $[BF_4]^-$ anions are elongated ((**1**) 1.470 [1.462] Å; (**2**) 1.464 [1.462] and 1.466 [1.457] Å) relative to the terminal B−F bonds ((**1**) 1.357 [1.353] Å; (**2**) 1.356 [1.352] and 1.365 [1.356] Å). The F(11)−Xe(1)−F(12) angles are comparable in (**2**) (166.6 [164.2]°) and (**1**) (161.8 [161.7]°), but are smaller than those of the isolated $[C_6F_5XeF_2]^+$ cation (178.3 [177.8]°) showing the sensitivity of this angle to coordination. This sensitivity is also apparent in the crystal structures of the $[C_6F_5XeF_2]^+$ salts (see X-ray Crystal Structures) and the N-base adducts of $C_6F_5IF_2$.[41] The calculated F(11)−Xe(1)−F(12) angles are slightly underestimated when compared with the experimental angles. The calculations show that the F−Xe−C_i−$C^{2,6}$ dihedral angle is also sensitive to coordination. In the calculated and experimental structures of (**2**), the F−Xe−C_{ipso}−$C^{2,6}$ dihedral angles deviate from 90° (calcd, 79.6 [65.5]°; exptl, 68.3(3)°). The calculated dihedral angle of (**1**) (90.0 [90.0]°) is significantly larger than in the experimental structure (67.5(2)°), where the dihedral angle is most likely affected by dimer formation between adjacent $[C_6F_5XeF_2]^+$ cations (Figure 3). It is also noteworthy that the relative orientations of the cation and the anion in the calculated $[C_6F_5XeF_2][BF_4]$ ion pair are such that avoidance of the xenon valence electron lone pairs is maximized; that is, the C(1), Xe(1), F(11), F(12)- and the F(13), B(1), F(14)-planes are coplanar (Figure 8a). The observed trends among the angles subtended at xenon are well-reproduced; in particular, F(13)---Xe(1)---F(14) in (**1**) (54.1 [54.6]°) is less than F(17)---Xe(1)---F(18) in (**2**) (69.7 [70.4]°).

(ii) $[C_6F_5XeF_2]^+$ and $C_6F_5IF_2$. The calculated Xe−C and I−C bond lengths are essentially equal (Xe, 2.090 [2.056] Å; I, 2.090 [2.067] Å), in agreement with the observed average bond lengths (Xe, 2.058(2)−2.058(3) Å; I, 2.068(3), 2.068(4) Å). Although both the Xe−F and I−F bond lengths are slightly overestimated, the experimental trend, Xe−F < I−F, is reproduced (calcd: Xe, 1.963 [1.938] Å and I, 2.009 [1.986] Å; exptl: Xe, 1.925(2)−1.948(2) Å and I, 1.950(3)−2.032(2) Å). The calculations also reproduce the experimental F−Xe−F angles ((**1**): 170.22(7); (**2**): 168.7(1); (**3a**): 170.5(1); (**3b**): 165.5(2) and 167.3(1)°) and F−I−F angles (170.46(10) and 171.59(9)°), which are bent toward the C_6F_5 groups. The calculated F−I−F angle (172.2 [171.3]°) is less than the calculated F−Xe−F angle (178.3 [177.8]°. The larger calculated F−Xe−F angle is consistent with the more contracted xenon lone pair domains in $[C_6F_5XeF_2]^+$, which are attributable to the higher positive Xe(IV) charge compared to that of I(III) (see Natural Bond Orbital Analyses). Although the calculated F−I−F angle (172.2 [171.3]°) compares well with the experimental value (171.59(9)°), the calculated F−Xe−F angle (178.3 [177.8]°) is significantly more open than in the crystal structures of $[C_6F_5XeF_2][BF_4]$ (170.22(7)°), $[C_6F_5XeF_2][BF_4]\cdot 2HF$ (168.7(1)°), and $[C_6F_5XeF_2]^+\cdot 2NCCH_3$ (165.5(2)−170.5(1)°). Compressions of the F−Xe−F angles in the crystal structures likely occur to accommodate base ($[BF_4]^-$, CH_3CN, and $[BF_4]^-\cdot 2HF$) coordination to xenon and to provide better access to the σ Xe−F* antibonding orbitals (see Natural Bond Orbital (NBO) Analyses). The calculated F−Xe−C_{ipso}−$C^{2,6}$ and F−I−C_{ipso}−$C^{2,6}$ dihedral angles vary depending on the level of the calculation and on the basis set used. Although the $[C_6F_5XeF_2]^+$ cation could be optimized using C_{2v} symmetry with the XeF_2 group orientated perpendicular to the C_6F_5 group, $C_6F_5IF_2$ gave an energy-minimized geometry having C_2 symmetry and a F−I−C_{ipso}−$C^{2,6}$ dihedral angle of 92.8 [103.9]° (Table 6). Similar behavior was observed at the LANL2DZ/RHF level.[42] It is difficult to account for some differences between calculated and observed geometrical parameters. Although all crystal structures reveal several interionic/intermolecular contacts to xenon (see X-ray Crystal Structures) or iodine,[42] their numbers and strengths vary, likely influencing the local geometries at xenon and iodine.

(iii) $[C_6F_5XeF_2]^+\cdot CH_3CN$ (3a) and $[C_6F_5XeF_2]^+\cdot 2CH_3CN$ (3b). The calculated Xe−C bond lengths remain essentially unchanged upon coordination of one CH_3CN molecule, but elongate slightly for two coordinated CH_3CN molecules (calcd: $[C_6F_5XeF_2]^+$, 2.090 [2.056] Å; (**3a**), 2.088 [2.058] Å; (**3b**), 2.106 [2.073] Å; exptl: (**3a**), 2.067(4) Å; (**3b**), 2.066(5) and 2.083(5) Å). The calculated Xe−F bond lengths elongate slightly upon coordination to one or two CH_3CN molecules ($[C_6F_5XeF_2]^+$, 1.963 [1.938] Å; (**3a**), 1.975 [1.949] Å; (**3b**), 1.978 [1.953] Å), reproducing the observed behavior ((**3a**), 1.930(2) and 1.939(2) Å; (**3b**), 1.940(2) and 1.940(2) Å). The calculated Xe---N contact distances also increase with the number of CH_3CN molecules ((**3a**), 2.691 [2.673] Å; (**3b**), 2.795 [2.764] Å), in agreement with the experimental trends ((**3a**), 2.742(4) Å; (**3b**), 2.816(4) and 2.868(4) Å). The calculated Xe−C and Xe−F bond lengths of $[C_6F_5XeF_2]^+\cdot 2CH_3CN$ are slightly overestimated when compared with the experimental values of $[C_6F_5XeF_2][BF_4]\cdot 2CH_3CN$, whereas the calculated Xe---N contact distances are slightly underestimated. The F−Xe−F angles decrease as the xenon coordination number increases, with calculated F−Xe−F values for one CH_3CN (177.1 [176.4]°) and two CH_3CN molecules (164.5 [165.1]°) that are close to those in the crystal structures ((**3a**), 170.5(1)°; (**3b**), 165.5(2), 167.3(1)°). The calculated F−Xe−C_{ipso}−$C^{2,6}$ dihedral angles vary only slightly with the number of coordinated CH_3CN molecules (90.2 [90.0]° for one CH_3CN molecule; 88.6 [82.3]° for two CH_3CN molecules). The calculated N---Xe---N and C−Xe---N angles in $[C_6F_5XeF_2]^+\cdot 2CH_3CN$ are 66.4 [66.7]° and 146.8 [146.7]°, respectively, in good agreement with experiment (63.6(1) and 64.6(1)°; 148.20(8) and 147.71(8)°, respectively). The Xe---N−C angles are close to linear in $[C_6F_5XeF_2]^+\cdot CH_3CN$ (179.8 [180.0]°), but are significantly bent in $[C_6F_5XeF_2]^+\cdot 2CH_3CN$ (169.1 [169.9]° and 169.0 [169.9]°). The differences between calculated and experimental values ((**3a**), 161.1(4)°; (**3b**), 153.1(4), 142.7(3)°) most likely result from crystal packing.

(b) Natural Bond Orbital (NBO) Analyses; Charges, Valencies, and Bond Orders. The NBO[63] analyses of

dx.doi.org/10.1021/ic501831j | Inorg. Chem. XXXX, XXX, XXX−XXX

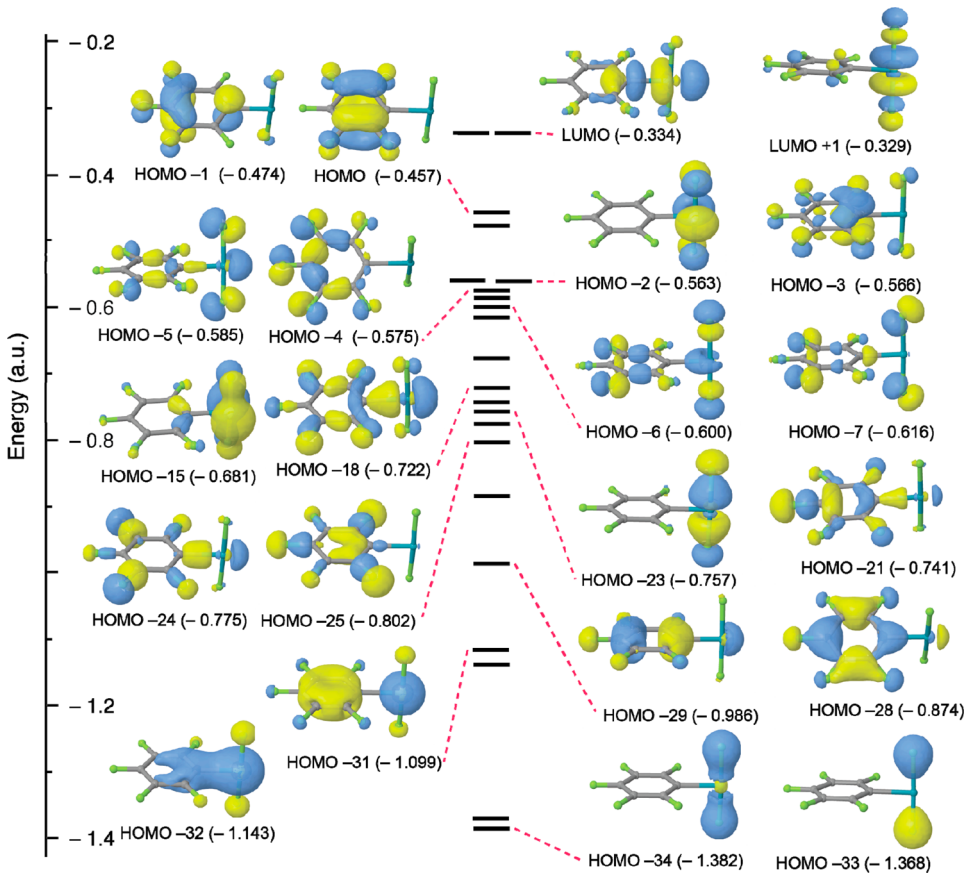

Figure 9. Energies and molecular orbitals of $[C_6F_5XeF_2]^+$ ranging from LUMO +1 to HOMO −7 and selected orbitals having >5% Xe−C/F or Xe lone pair character (B3LYP/aug-cc-pVTZ).

$[C_6F_5XeF_2]^+$, $[C_6F_5XeF_2]^+\cdot CH_3CN$, $[C_6F_5XeF_2]^+\cdot 2CH_3CN$, $C_6F_5IF_2$, and the ion pairs, $[C_6F_5XeF_2][BF_4]$ and $[C_6F_5XeF_2][BF_4]\cdot 2HF$, were carried out for the optimized gas-phase structures and are compared with those of $[XeF_3]^+$, IF_3 $[C_6F_5Xe]^+$, $[C_6F_5Xe]^+\cdot CH_3CN$, C_6F_5I, $[XeF]^+$, C_6F_6, HF, and CH_3CN at the B3LYP and PBE1PBE/aug-cc-pVTZ(-PP) levels of theory (Supporting Information, Tables S13 and S14). Only the B3LYP values are referred to in the ensuing discussion.

The positive charges on Xe/I decrease with decreasing formal oxidation state within their respective C_6F_5- and fluoro-analogue series (Supporting Information, Table S13), that is, $[XeF_3]^+$ (2.311) and IF_3 (1.776); $[C_6F_5XeF_2]^+$ (1.934) and $C_6F_5IF_2$ (1.490); $[XeF]^+$ (1.338) and IF (0.531); $[C_6F_5Xe]^+$ (0.885) and C_6F_5I (0.249). The *ipso*-carbon atoms of the Xe(IV) (−0.183 to −0.335), Xe(II) (−0.215 and −0.251), I(III) (−0.269), and I(I) (−0.234) derivatives bear substantial negative charges. The *ipso*-carbon charges of $[C_6F_5Xe]^+$ and $[C_6F_5XeF_2]^+$ are less negative than those of their less electrophilic neutral isoelectronic I(I) and I(III) analogues. The negatively charged *ipso*-carbons are indicative of ring charge migration in both the xenon and iodine derivatives. The charges on $C^{2,6}$, $C^{3,5}$, and C^4 are positive for Xe(IV) (0.421−0.283), Xe(II) (0.312−0.352), I(III) (0.288−0.326), and I(I) (0.287−0.305), reflecting the greater inductive effects of xenon on the C_6F_5-ring. Overall, the charges on the carbon atoms of $[C_6F_5XeF_2]^+$, $C_6F_5IF_2$, $[C_6F_5Xe]^+$, and C_6F_5I alternate as follows; $C_{ipso} < C^{3,5} < C^{2,6} < C^4$. These charge distributions are significantly influenced by the C_6F_5 group, which favors higher positive charges on the $C^{2,6}$ and C^4 atoms. The $[C_6F_5XeF_2]^+$ and $[C_6F_5Xe]^+$ cations show nearly identical charges on the $C^{3,5}$ atoms (0.317 and 0.319), but the $C^{2,6}$ (0.345 and 0.322) and C^4 (0.377 and 0.352) atoms are more positively charged in $[C_6F_5XeF_2]^+$ than in $[C_6F_5Xe]^+$. Similarly, the $C^{3,5}$ atoms in $C_6F_5IF_2$ and C_6F_5I show charges of 0.288 and 0.287, but the $C^{2,6}$ (0.292 and 0.318) and C^4 (0.305 and 0.326) atoms are more positively charged in $C_6F_5IF_2$ than in C_6F_5I. The C_{ipso} atom is more negatively charged in $[C_6F_5XeF_2]^+$ (−0.255) than in $[C_6F_5Xe]^+$ (−0.215), and this trend also applies to $C_6F_5IF_2$ (−0.269) and C_6F_5I (−0.234). The total C_6F_5 group charges are positive for $[C_6F_5XeF_2]^+$ (0.171), $[C_6F_5Xe]^+$ (0.122), $[C_6F_5XeF_2]^+\cdot CH_3CN$ (0.083), and $[C_6F_5XeF_2]^+\cdot 2CH_3CN$ (0.045), whereas the C_6F_5 group charges of $[C_6F_5XeF_2][BF_4]$ (−0.056), $[C_6F_5XeF_2][BF_4]\cdot 2HF$ (−0.009), $[C_6F_5Xe]^+\cdot CH_3CN$ (−0.001), $C_6F_5IF_2$ (−0.183), and C_6F_5I (−0.249) are negative or close to zero. The C_6F_5 group charges of the xenon derivatives are not only influenced by the oxidation state of xenon but also significantly reduced by electron-pair donors coordinated to xenon. The negative C_6F_5 group charges of the neutral iodine analogues also reflect the formal oxidation state of the iodine atom.

The Xe^{IV}−C (0.633−0.740) and I^{III}−C (0.706) Mayer bond orders are approximately twice those of the more ionic Xe−F (0.360) and I−F (0.345) bonds of the XeF_2/IF_2 groups. The Xe^{II}−C bond orders of $[C_6F_5Xe]^+$ (0.714) and $[C_6F_5Xe]^+\cdot CH_3CN$ (0.676) and the I^{I}−C bond order of C_6F_5I (0.746) also display the same trend, I(I) > Xe(II) and I(III) > Xe(IV), reflecting the greater ionic characters of the Xe−C bonds for both pairs of isoelectronic species. The Xe−C bond order of $[C_6F_5XeF_2]^+$ (0.740) is only slightly higher than that of $[C_6F_5Xe]^+$ (0.714). As expected, the Xe−C bond order

dx.doi.org/10.1021/ic501831j | Inorg. Chem. XXXX, XXX, XXX−XXX

decreases slightly upon complexation ($[C_6F_5XeF_2]^+$ 0.740; $[C_6F_5XeF_2]^+\cdot 2CH_3CN$ 0.690; $[C_6F_5XeF_2]^+\cdot CH_3CN$ 0.667; $[C_6F_5XeF_2][BF_4]$ 0.633; $[C_6F_5XeF_2][BF_4]\cdot 2HF$ 0.657). The small Xe---N bond orders of $[C_6F_5XeF_2]^+\cdot CH_3CN$ (0.101), $[C_6F_5XeF_2]^+\cdot 2CH_3CN$ (0.078), and $[C_6F_5Xe]^+\cdot CH_3CN$ (0.085) are in accordance with the small calculated ν(CN) complexation shifts (Supporting Information, Table S7). The xenon valency is very similar for $[C_6F_5XeF_2]^+$ (1.472) and $[C_6F_5XeF_2]^+\cdot CH_3CN$ (1.467) but is significantly greater for $[C_6F_5XeF_2]^+\cdot 2CH_3CN$ (1.560). The added valency contribution to xenon resulting from CH_3CN coordination is compensated for by decreases in the respective C_{ipso} atom valency and F_{Xe} atom valencies of $[C_6F_5XeF_2]^+\cdot CH_3CN$ (2.640 and 0.322) and $[C_6F_5XeF_2]^+\cdot 2CH_3CN$ (2.818 and 0.314) compared to those of $[C_6F_5XeF_2]^+$ (2.914 and 0.338).

The CH_3CN molecules coordinated to $[C_6F_5Xe]^+$ and $[C_6F_5XeF_2]^+$ show significant nitrogen and carbon atom charge polarizations for their CN groups relative to those of free CH_3CN, with nitrogen becoming more negative and carbon becoming more positive by about the same amounts upon coordination. The CH_3 group charges are little affected by coordination. The positive charges born by Xe(II) and Xe(IV) in the $[C_6F_5Xe]^+$ and $[C_6F_5XeF_2]^+$ adducts slightly increase upon coordination, and their corresponding C_6F_5 ring charges become more negative. The mutual polarizations of the xenon cations and their coordinated base molecules (HF and CH_3CN) and anions ($[BF_4]^-$ and $[BF_4]^-\cdot 2HF$) are reflected in their respective cation and CH_3CN ligand or $[BF_4]^-/[BF_4]^-\cdot 2HF$ anion charges: $[C_6F_5Xe]^+\cdot CH_3CN$ (0.934, 0.064), $[C_6F_5XeF_2]^+\cdot CH_3CN$ (0.939, 0.064), $[C_6F_5XeF_2]^+\cdot 2CH_3CN$ (0.913, 0.090), $[C_6F_5XeF_2][BF_4]\cdot 2HF$ (0.899, −0.899), and $[C_6F_5XeF_2][BF_4]$ (0.822, −0.829) and correspond to negative charge transfers from the base to the $[C_6F_5XeF_2]^+$ cation of −0.064, −0.064, −0.090, −0.101, and −0.171, respectively. The Xe---N and Xe---F donor−acceptor interactions display small Xe---N bond orders for the CH_3CN complexes with $[C_6F_5XeF_2]^+$ (0.078−0.101) and $[C_6F_5Xe]^+$ (0.085) and similar Xe---F bridge bond orders for the $[C_6F_5XeF_2]^+$ ion pairs with $[BF_4]^-$ (0.084) and $[BF_4]^-\cdot 2HF$ (0.069, 0.061).

(c) Bonding. The bonding of the T-shaped CXF_2 group (X = Xe(IV), I(III)) in $[C_6F_5XeF_2]^+$ and $C_6F_5IF_2$ can be described in terms of a 3c−4e bond for the nearly linear *trans*-axial F−X−F group and a 2c−2e bond for the equatorial C−X bond. The 3c−4e bond can be viewed as a linear combination of a filled pure Xe/I 5p orbital that overlaps with two half-filled 2p orbitals of the axial fluorine ligands. The occupied nonbonding molecular orbital has mainly ligand character, which accounts for the high electron densities on the fluorine atoms of the XeF_2/IF_2 groups. The Xe−F bonding is mixed into five orbitals corresponding to HOMO −6, −7, −23, −33, and −34 (Figure 9). The bonding is essentially p in character for Xe (ca. 97% p) and F (6% s and 93% p). The charges on the axial fluorine ligands bonded to Xe(IV) in $[C_6F_5XeF_2]^+$ and its various base complexes fall into a narrow range (−0.554 to −0.573) and are less negative than those of $C_6F_5IF_2$ (−0.653).

The Xe−C σ bond results from the interaction of a Xe p-orbital (13% s, 86% p) and a C p-orbital (20% s, 77% p), with a slightly higher polarization coefficient for Xe that corresponds to its higher electronegativity relative to that of carbon. The σ I−C bond of $C_6F_5IF_2$ has very similar hybridizations for I (12% s, 87% p) and C (23% s, 76% p), but the more electronegative carbon atom has a higher polarization coefficient than iodine. The Xe−C bonding NBO is distributed over six orbitals and contributes 8, 29, 8, 14, 7, and 17% to HOMO −5, −18, −21, −24, −28, and −32, respectively (Figure 9). The bonding and lone pair NBOs of $C_6F_5IF_2$ are very similar in character to those of $[C_6F_5XeF_2]^+$, but their MO mixings are significantly different as a consequence of the different orbital energies.

The LUMO and LUMO +1 of the $[C_6F_5XeF_2]^+$ cation represent its electrophilic behavior and are mainly σ Xe−C* (−0.334 au) and σ Xe−F* (−0.329 au) in character, respectively (Figure 9). The HOMO (−0.457 au) and HOMO −1 (−0.474 au) are nearly degenerate and mainly consist of π orbitals centered on the carbon and fluorine atoms of the C_6F_5 group. The frontier orbitals of $C_6F_5IF_2$ are similar to those of $[C_6F_5XeF_2]^+$ but are higher in energy and include a HOMO −1 comprised of I and F lone-pair density (Supporting Information, Figure S9). In comparison, the $[XeF_3]^+$ cation contains HOMO and LUMO orbitals with energies (−0.625 and −0.464 au, respectively) that are substantially lower than those of the $[C_6F_5XeF_2]^+$ cation. Higher orbital energies of $[C_6F_5XeF_2]^+$ are anticipated because of the lower electron-withdrawing strength of the C_6F_5 group relative to that of fluorine. The HOMO/LUMO energy gap of $[C_6F_5XeF_2]^+$ (0.123 au) is less than those of $[XeF_3]^+$ (0.161 au) and its isoelectronic iodine analogue, $C_6F_5IF_2$ (0.197 au).

The crystal structure of $[C_6F_5XeF_2][BF_4]\cdot 1.5CH_3CN$ shows two coordination behaviors for $[C_6F_5XeF_2]^+$, the nearly linear C−Xe−N arrangement in $[C_6F_5XeF_2]^+\cdot CH_3CN$ and a distorted pentagonal planar arrangement of C_{ipso}, 2F, and 2N atoms around Xe in $[C_6F_5XeF_2]^+\cdot 2CH_3CN$. Neglecting Xe---F interactions involving the $[BF_4]^-$ anions, the Xe−N donor−acceptor interactions of the gas-phase $[C_6F_5XeF_2]^+\cdot CH_3CN$ and $[C_6F_5XeF_2]^+\cdot 2CH_3CN$ cations were investigated. The nitrogen lone pair of the adduct cation, $[C_6F_5XeF_2]^+\cdot CH_3CN$, overlaps with the σ Xe−C* orbital to provide a stabilization of 32.1 kJ mol^{-1}, but does not interact with the orthogonal σ Xe−F* orbitals (Figure 10a). The nitrogen atom lone pairs of

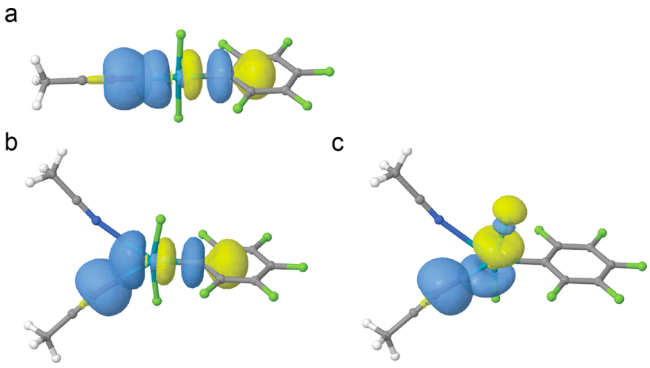

Figure 10. Selected prenormalized NBOs for (a) the $[C_6F_5XeF_2]^+\cdot CH_3CN$ and (b, c) $[C_6F_5XeF_2]^+\cdot 2CH_3CN$ cations which have significant N−Xe bonding interactions (B3LYP/aug-cc-pVTZ).

$[C_6F_5XeF_2]^+\cdot 2CH_3CN$ are orientated such that each nitrogen atom donates density into the σ Xe−C* orbital as well as into both σ Xe−F_1* and σ Xe−F_2* orbitals, providing 14.1, 4.4, and 1.1 kJ mol^{-1} of stabilization (Figure 10b,c; the least stable N:→ Xe−F* NBO is not shown). The natural linear molecular orbital (NLMO) analysis of these adducts shows 1−2% mixing of the Xe and C orbitals with the N valence electron lone pairs. Similar geometries and donor−acceptor behaviors were observed for $[C_6F_5XeF_2][BF_4]$ and $[C_6F_5XeF_2][BF_4]\cdot 2HF$

dx.doi.org/10.1021/ic501831j | Inorg. Chem. XXXX, XXX, XXX−XXX

and in the crystal structures of $C_6F_5IF_2$ with adducted nitrogen bases.[41]

Two lone-pair NBOs are present on the Xe atom of $[C_6F_5XeF_2]^+$, where one lone pair NBO is ca. 87% s and 13% p character, and the other is >99% p character. The lone pair of greater p-character is approximately perpendicular to the Xe−C and Xe−F bonds and is a contributor to HOMO −2 (55%) and HOMO −15 (36%) along with the lone pairs of the axial fluorine atoms. The lone pair having mainly s character is oriented at ca. 180° with respect to the Xe−C bond and mixes with six orbitals. This lone pair contributes 6, 6, 7, 19, 32, and 11% to HOMO −5, −18, −29, −31, −32, and −34, respectively.

EXPERIMENTAL SECTION

General. *(a) Apparatus.* Manipulations involving air-sensitive materials were carried out under anhydrous conditions on glass and metal high-vacuum lines as previously described.[64] Solid, low-volatility, and moisture-sensitive materials were handled inside a drybox (Vacuum Atmospheres Model DLX, nitrogen atmosphere or Braun equipped with a MB 100G gas purification unit, argon atmosphere). Reaction vessels were constructed from 23-, 8.0-, and 3.5-mm i.d. tetrafluoroethylenehexafluoropropylene block copolymer (FEP) tubing and were dried under dynamic vacuum for several hours prior to use. Vessels used for low-temperature crystallization were constructed from $^1/_4$-in. o.d. ($^1/_{16}$-in. wall thickness) lengths of FEP tubing. The tubing was heat-sealed at one end, heat flared at the other end, and connected through a 45° SAE flare nut to the conical end of a chlorotrifluoroethylene polymer (Kel-F) valve to form a compression seal. Prior to use, the vacuum-dried reaction vessels were passivated for at least 8 h with 1 atm of F_2 gas. Vacuum line connections were made using $^1/_4$-in. 316 stainless steel Swagelok Ultratorr unions fitted with Viton O-rings.

(b) Materials. Acetonitrile[65] (Caledon, HPLC grade), CH_2Cl_2[40] (Caledon, reagent grade), and SO_2ClF[66] (Allied Chemical, Baker and Adams Division) were purified by the literature methods and stored over 3 Å molecular sieves. 1,1,1,3,3-Pentafluorobutane (Solvay, >99.5%) was refluxed over P_4O_{10} and stored over 3 Å molecular sieves. Anhydrous HF (Harshaw Chemicals Co.) was purified in a nickel vessel by exposure to F_2 gas at room temperature as previously described.[67] Anhydrous HF was then vacuum-distilled into a dry Kel-F storage vessel equipped with a Kel-F valve and stored at room temperature until used. Anhydrous HF was dispensed by vacuum distillation into FEP reaction vessels or NMR sample tubes. Alternatively, aHF was purified in an electrochemical cell equipped with Ni anodes using a voltage of 4.5−5.5 V and a current density of 0.20−0.35 A dm^{-3} for 50 to 130 h before being transferred to a high-density polyethylene, FEP, or poly(tetrafluoroethylene) (PTFE) storage vessel and stored inside a freezer at −18 °C.[68] Portions of aHF were transferred from the storage vessel to reaction vessels through PTFE cannulas using a low pressure of dry argon.[40] The reagents C_6F_5Br (Institute of Organic Chemistry, Novosibirsk, 99%) and C_6F_5I (Bristol Organics Ltd.) were dried over 3 Å molecular sieves (Bayer AG, 3 Å). Xenon tetrafluoride was prepared according to the literature method.[69] Small amounts of XeF_6 contaminant were flash distilled from the bulk sample at room temperature. The purity of XeF_4 was assessed by low-temperature Raman spectroscopy, which showed that XeF_2 and XeF_6 were absent. The compounds $C_6F_5IF_2$,[42] $P(C_6F_5)_3$,[70,71] $As(C_6F_5)_3$,[71] $Bi(C_6F_5)_3$,[72,73] $K[C_6F_5BF_3]$,[74] and $C_6F_5BF_2$[74] were prepared as previously described.

The salt, $[C_6F_5XeF_2][BF_4]$ (vide infra), was transferred as a solid in a drybox equipped with a cryowell at ca. −140 °C using a precooled solid syringe, or under argon as a suspension in CH_2Cl_2, or as solutions in CH_3CN or aHF (−40 to −78 °C) through 1.5-mm o.d. PTFE cannulas as previously described.[40] The solid syringe consisted of a length of 2.0-mm o.d. FEP tubing and a 1.5 mm o.d. nickel rod, which served as the piston. Samples for long-term studies were stored in PTFE-stoppered FEP tubes inside a rigorously dried, argon-flushed glass vessel to minimize water diffusion through the FEP walls and PTFE stoppers. Samples were shielded from light and were periodically agitated. Reaction progress was monitored by ^{19}F and ^{129}Xe NMR spectroscopy at −40 or −78 °C. The total fluorine-atom-weighted integrated ^{19}F intensities of the C_6F_5 groups and their derivatives were set equal to 100 mol%. The mole percentages of non-C_6F_5 derivatives are reported relative to those of C_6F_5 compounds.

In the reactivity and long-term stability studies, $[C_6F_5XeF_2][BF_4]$ (100−150 mg; 0.48−0.72 mmol) was dissolved in the desired solvent (CH_3CN or aHF 400−1000 μL) at −40 or −78 °C, respectively. The solution was then split into two to four equal portions. One portion was initially checked for impurities and to establish the initial solution composition by recording its ^{11}B, ^{19}F, and ^{129}Xe NMR spectra at −40 °C.

Caution! *Anhydrous HF must be handled using appropriate protective gear with immediate access to proper treatment procedures*[75−77] *in the event of contact with liquid HF, HF vapor, or HF-containing solutions. The pure, light yellow solid, $[C_6F_5XeF_2][BF_4]$, is shock sensitive. Explosions of the solid have occurred at −78 °C without leaving a residue when samples were impacted by an FEP rod (ca. 3 g) dropped from a height of ca. 6 cm or by rapid pressurization of the evacuated reaction tube with dry argon gas to ca. 1 atm. Solvent-free $[C_6F_5XeF_2][BF_4]$ decomposes explosively when mechanically shocked at temperatures as low as −140 °C. Although samples of $[C_6F_5XeF_2][BF_4]$ containing unreacted XeF_4 did not decompose explosively at −40 °C, even when the solid was pulverized by striking the outside of the FEP storage vessel with a wooden dowel, extreme care must nevertheless be taken when handling $[C_6F_5XeF_2][BF_4]$ and mixtures containing this compound.*

Synthesis of $[C_6F_5XeF_2][BF_4]$. In a typical synthesis, XeF_4 (0.2132 g; 1.03 mmol) was suspended in cold (−78 °C) CH_2Cl_2 (20 mL) in a 23-mm i.d. FEP reaction vessel. A freshly prepared, cold (−78 °C) $C_6F_5BF_2$ solution (1950 μL; 1.03 mmol) was added to a vigorously stirred XeF_4 suspension at −78 °C and stirred for a further 15 min. The temperature was then raised to −55 °C, whereupon a voluminous yellow solid precipitated. After 1 h of additional stirring at −55 °C, the suspension was centrifuged at −78 °C, and the CH_2Cl_2 supernatant was removed under dry argon through a cannula as previously described.[40] The pale yellow solid was dried under dynamic vacuum (ca. 10^{-3} to 10^{-4} mbar) at temperatures below −55 °C, yielding pale yellow microcrystalline $[C_6F_5XeF_2][BF_4]$. The salt, $[C_6F_5XeF_2][BF_4]$, is very soluble in CH_3CN (−40 °C) or aHF (−78 °C). Such solutions contained ca. 6 mol% of by-products (mostly C_6F_6), which were present immediately after dissolution.

^{19}F NMR (282.40 MHz, aHF, −80 °C): −33.1 (s with ^{129}Xe-satellites: $^1J(^{19}F-^{129}Xe)$ = 3891 Hz, $RXeF_2$, 2F), −123.6 (mult, *o*-C_6F_5, 2F), −129.3 (tt, $^3J(^{19}F-^{19}F)$ = 18 Hz, $^4J(^{19}F-^{19}F)$ = 9 Hz, *p*-C_6F_5, 1F), −148.3 (quar., $^1J(^{11}B-^{19}F)$ = 12 Hz, 4F), −150.4 ppm (mult., *m*-C_6F_5, 2F). ^{11}B NMR (96.29 MHz): −1.3 ppm (quin, $^1J(^{11}B-^{19}F)$ = 11 Hz). ^{129}Xe NMR (83.02 MHz): −1765.9 ppm (t, $^1J(^{19}F-^{129}Xe)$ = 3894 Hz).

^{19}F NMR (282.40 MHz, CH_3CN, −40 °C): −27.7 ppm (s with ^{129}Xe-satellites: $^1J(^{19}F-^{129}Xe)$ = 3910 Hz, 2F), −124.1 ppm (mult, *o*-C_6F_5, 2F), −133.9 ppm (t, $^3J(^{19}F-^{19}F)$ = 20 Hz, *p*-C_6F_5, 1F), −147.1 ppm (s, $\Delta\nu_{^1/_2}$ = 4 Hz, $^{11}BF_4$, 4F), −154.3 ppm (mult, *m*-C_6F_5, 2F). ^{11}B NMR (96.29 MHz): −0.6 ppm (quin, $^1J(^{11}B-^{19}F)$ = 11 Hz). ^{129}Xe NMR (83.02 MHz): −1701.3 ppm (t, $^1J(^{129}Xe-^{19}F)$ = 3881 Hz).

Stabilities of $[C_6F_5XeF_2][BF_4]$ in aHF or CH_3CN Solutions. Long-term stability studies were carried out on solutions of $[C_6F_5XeF_2][BF_4]$ (0.10−0.35 mmol) in aHF or CH_3CN (400−600 μL) contained in a 3.5-mm i.d. FEP reaction vessels that also served as NMR sample tubes when inserted into 5-mm o.d. Pyrex glass NMR tubes. The initial solution compositions were established by ^{11}B, ^{19}F, and ^{129}Xe NMR spectroscopy at −78 °C (aHF) or −40 °C (CH_3CN). The solution was subsequently allowed to warm to the desired temperature (−40, −30 °C, or room temperature). The samples were monitored by ^{19}F NMR spectroscopy at −78 or −40 °C. For low-temperature studies, the samples contained in a glass trap filled with dry argon gas, were placed in a cryostat set to the desired temperature.

dx.doi.org/10.1021/ic501831j | Inorg. Chem. XXXX, XXX, XXX−XXX

Reactions of $[C_6F_5XeF_2][BF_4]$ with the Pnictogen(III) Compounds, $Pn(C_6F_5)_3$ (Pn = P, As, and Bi) in CH_3CN. In a 3.5-mm i.d. FEP reaction vessel, $Pn(C_6F_5)_3$ (Bi, 95.89 mg, 0.142 mmol; As, 143.46 mg, 0.251 mmol; P, 133.49 mg, 0.25 mmol), was dissolved or, in the cases of the arsenic and phosphorus compounds, suspended in CH_3CN (1000 μL) and then cooled to −78 °C. Quantities of cold (−40 °C) CH_3CN solutions of $[C_6F_5XeF_2][BF_4]$ (ca. 50 mg, 0.25 mmol) were added to the CH_3CN solutions/suspensions of $Pn(C_6F_5)_3$ and allowed to warm to −40 °C. Yellow suspensions of $P(C_6F_5)_3$ and $As(C_6F_5)_3$ turned white after 40 min at −40 °C. The progress of each reaction was monitored by ^{19}F NMR spectroscopy at −40 °C. The resulting white suspensions were dissolved at room temperature and analyzed by ^{19}F NMR spectroscopy (24 °C) to determine the reaction product distributions.

$P(C_6F_5)_3F_2$ (282.40 MHz, CH_3CN, −40 °C). ^{19}F NMR: −2.0 ppm (d, $^1J(^{19}F-^{35}P)$ = 681 Hz, 2F), −132.6 ppm (mult, *o*-C_6F_5, 6F), −145.3 ppm (t, $^3J(^{19}F-^{19}F)$ = 20 Hz, *p*-C_6F_5, 3F), −158.1 ppm (mult, *m*-C_6F_5, 6F)

$As(C_6F_5)_3F_2$ (282.40 MHz, CH_3CN, −40 °C). ^{19}F NMR: −23.6 ppm (mult, 2F), −132.6 ppm (mult, *o*-C_6F_5, 6F), −145.3 ppm (t, $^3J(^{19}F-^{19}F)$ = 20 Hz, *p*-C_6F_5, 3F), −158.1 ppm (mult, *m*-C_6F_5, 6F)

$Bi(C_6F_5)_3F_2$ (282.40 MHz, CH_3CN, −40 °C). ^{19}F NMR: −60.5 ppm (s, $\Delta\nu_{1/2}$ = 49 Hz, BiF_2, 2F), −126.3 ppm (mult, *o*-C_6F_5, 6F), −142.6 ppm (t, $^3J(^{19}F-^{19}F)$ = 21 Hz, *p*-C_6F_5, 3F), −154.4 ppm (mult, *m*-C_6F_5, 6F)

Reactions of $[C_6F_5XeF_2][BF_4]$ with C_6F_5X (X = Br or I) in CH_3CN and aHF. In a 3.5-mm i.d. FEP reaction vessel, C_6F_5Br (20 μL, 0.16 mmol) was dissolved in CH_3CN (100 μL) and cooled (−40 °C). A cold (−40 °C) CH_3CN (800 μL) solution of $[C_6F_5XeF_2][BF_4]$ (ca. 50 mg, 0.25 mmol) was added to the C_6F_5Br solution at −40 °C. The reaction mixture was maintained for ca. 18 h at −40 to −54 °C. No reaction was evident when the ^{19}F NMR spectrum was periodically monitored at −40 °C.

The salt, $[C_6F_5XeF_2][BF_4]$, (ca. 25 mg, 0.12 mmol) was dissolved in cold (−78 °C) aHF (500 μL) and initially checked by ^{19}F NMR spectroscopy at −80 °C to establish its purity. Approximately an equimolar amount of C_6F_5Br (mp −31 °C; 15 μL, 0.12 mmol) was added to the aHF solution of $[C_6F_5XeF_2][BF_4]$ at −40 °C, and the mixture was maintained for 2 h at this temperature. Although C_6F_5Br is practically insoluble in aHF and frozen at −40 °C, it was detected in the aHF supernatant. The sample was stored for 4 d under argon inside a glass tube at −78 °C, but no reaction between $[C_6F_5XeF_2][BF_4]$ and C_6F_5Br ensued. Iodopentafluorobenzene, C_6F_5I (20 μL; 0.15 mmol), was added to the sample at −40 °C. The compound, C_6F_5I, has a melting point of −29 °C and a very low solubility in aHF. During the course of the reaction, the sample was maintained at −40 °C for 30 min. $C_6F_5IF_2$ (282.40 MHz, aHF, −80 °C): ^{19}F NMR: −119.6 ppm (mult, *o*-C_6F_5, 2F), −138.3 ppm (tt, $^3J(^{19}F-^{19}F)$ = 19 Hz, $^4J(^{19}F-^{19}F)$ = 8 Hz, *p*-C_6F_5, 1F), −154.9 ppm (mult, *m*-C_6F_5, 2F), −177.4 ppm (s, $\Delta\nu_{1/2}$ = 723 Hz, 2F).

Reactivity of $[C_6F_5XeF_2][BF_4]$ with $[C_6F_5BF_3]^-$. The salt, $K[C_6F_5BF_3]$ (100 mg; 0.36 mmol), was suspended in cold (−80 °C) aHF (400 μL) inside a 3.5-mm i.d. FEP reaction tube. A cold (−40 °C) aHF solution of $[C_6F_5XeF_2][BF_4]$ (ca. 50 mg, 0.25 mmol) was added to the suspension. The reaction mixture was maintained at −40 °C for 30 min and was monitored by ^{19}F NMR spectroscopy (−40 °C).

The salt $K[C_6F_5BF_3]$ (25.00 mg; 0.09 mmol) was suspended in CH_3CN (300 μL) inside a 3.5 mm i.d. FEP reaction tube and cooled to −40 °C. A cold (−40 °C) CH_3CN solution of $[C_6F_5XeF_2][BF_4]$ (ca. 50 mg, 0.25 mmol) was added to the $K[C_6F_5BF_3]$ suspension in CH_3CN. The sample was maintained at −40 °C for 140 h and was monitored by ^{19}F NMR spectroscopy (−40 °C).

NMR Spectroscopy. *(a) Instrumentation and Spectral Acquisition Parameters.* NMR spectra were measured in 18.5-cm lengths of 4.1-mm o.d. × 3.5-mm i.d. FEP tubing that were sealed at one end, closed with PTFE plugs at the other end, and placed inside a thin-walled precision Pyrex glass NMR tubes (Wilmad 537 PPT), which contained CD_2Cl_2 or CD_3CN as the deuterium-lock substance in the annular space, or internally as dry solvents in precision glass NMR tubes. Ambient (24 °C) and low-temperature NMR spectra were recorded in the deuterium-locked mode on a Bruker Avance 300 spectrometer equipped with a 7.0463 T cryomagnet. For low-temperature work, the NMR probe was cooled using a nitrogen flow and a variable-temperature controller (BVT 3000).

The ^{19}F NMR spectra were acquired using a 5-mm combination $^1H/^{19}F$ probe operating at 282.40 MHz. The ^{11}B and ^{129}Xe NMR spectra were obtained using a 5-mm broad-band inverse probe operating at 96.29 and 83.02 MHz. Pulse widths, corresponding to bulk magnetization tip angles of ca. 90°, were 9.3 (^{11}B), 14.6 (^{19}F), and 8.5 (^{129}Xe) μs. Line-broadening parameters used in exponential multiplication of the free induction decays were set equal to or less than their respective data-point resolutions or the natural line widths of the resonances. All line-shape functions were Lorentzian unless specified otherwise. In some cases, the free induction decays were multiplied by Gaussian functions for resolution enhancement upon Fourier transformation. Spectra were recorded using optimal memory sizes, acquisition times, and relaxation delays (0.5−2 s).

All chemical shifts were referenced with respect to their respective standards at 24 °C. The ^{19}F NMR spectra were referenced to CCl_3F using either the internal standards C_6F_6 (−162.9 ppm) or $C_6H_5CF_3$ (−63.9 ppm) or externally to neat CCl_3F. The ^{129}Xe NMR spectra were referenced externally to liquid $XeOF_4$ or indirectly by use of the secondary external reference XeF_2/CD_3CN extrapolated to zero concentration, yielding an XeF_2 chemical shift of −1813.3 ppm relative to external liquid $XeOF_4$.[78] The ^{11}B NMR spectra were referenced to external $BF_3{\cdot}Et_2O$ (neat) or to an external $BF_3{\cdot}Et_2O/CD_3Cl$ solution (15% v/v). A positive (negative) sign denotes a chemical shift to high (low) frequency of the reference compound.

(b) Simulation of NMR Spectra. The ^{19}F and ^{129}Xe NMR spectra of the $[C_6F_5XeF_2]^+$ cation and of the isoelectronic $C_6F_5IF_2$ molecule were simulated using the programs *gNMR*[43] and *ISOTOPOMER*.[44] The programs provided heteronuclear simulations that took into account the natural abundance of ^{129}Xe ($I = {}^1/_2$, 26.44%). The $J(^{19}F-^{131}Xe)$ couplings were assumed to be quadrupole collapsed ^{131}Xe ($I = {}^3/_2$, 21.23%) due to the asymmetry of the electric field at the xenon nucleus.

Raman Spectroscopy. *(a) Raman Sample Preparation.* The Raman spectrum of the pale yellow solid, $[C_6F_5XeF_2][BF_4]$, was measured in a precision Pyrex glass NMR tube (Wilmad 507) fused to a $^1/_4$-in. o.d. length of Pyrex glass tubing that was, in turn, connected to a J. Young stopcock by means of a $^1/_4$-in. 316 stainless steel Swagelok Ultratorr union outfitted with Viton O-rings. The assembly was opened inside the drybox, and the compound was loaded into the sample tube (ca. −140 °C) by use of a solid syringe (vide supra). To avoid temperature shock and sample detonation, the bottom portion of the syringe was precooled to −140 °C immediately prior to insertion into the bulk sample, filled, and rapidly transferred into the cold (−140 °C) NMR tube. The J. Young valve assembly was reconnected to the sample tube and removed cold from the drybox. The sample was cooled to −196 °C, evacuated, heat sealed, and stored at −196 °C until its Raman spectrum could be recorded. The Raman spectrum of bright yellow, solid $[C_6F_5XeF_2][BF_4]{\cdot}2HF$ was measured directly in the $^1/_4$-in. o.d. FEP reaction tube and Kel-F valve assembly that was used for its synthesis.

(b) Raman Instrumentation and Spectral Acquisition. The low-temperature (−150 °C) Raman spectrum was recorded on a Bruker RFS 100 FT Raman spectrometer using 1064-nm excitation at 350 mW and a resolution of 1 cm^{-1} as previously described.[79] A total of 2000−2400 scans were recorded.

X-ray Crystallography. Each crystallization commenced from a suspension of $[C_6F_5XeF_2][BF_4]$ in CH_2Cl_2, which was transferred under argon at −78 °C by means of an FEP cannula into a dry $^1/_4$-in. o.d. T-shaped FEP vessel and connected to a Kel-F valve. Following crystal growth, suitable crystals were selected in a dry nitrogen cold stream at −110 ± 3 °C and were mounted on a goniometer head in a nitrogen cold stream (−173 °C) as previously described.[79]

*(a) Crystal Growth. (i) $[C_6F_5XeF_2][BF_4]$ (**1**).* On a glass vacuum line, CH_3CN (0.8 mL) was condensed at −196 °C onto a suspension of

dx.doi.org/10.1021/ic501831j | Inorg. Chem. XXXX, XXX, XXX−XXX

$[C_6F_5XeF_2][BF_4]$ (ca. 100 mg, 0.24 mmol) in CH_2Cl_2 (0.5 mL) to give a partially soluble yellow suspension at −40 °C. The reaction vessel was pumped under dynamic vacuum at −55 °C until enough CH_2Cl_2 was removed to completely dissolve all of the $[C_6F_5XeF_2][BF_4]$ (final volume, ca. 0.8 mL). The reactor was then pumped to dryness under dynamic vacuum at −40 °C over a period of 18 h to yield yellow plates. The crystal that was mounted had the dimensions of 0.27 × 0.14 × 0.08 mm^3.

*(ii) $[C_6F_5XeF_2][BF_4]\cdot 2HF$ (**2**).* Methylene chloride was removed from a suspension of $[C_6F_5XeF_2][BF_4]$ (~0.05 g, ~0.1 mmol) in CH_2Cl_2 (0.4 mL) under dynamic vacuum at −55 to −45 °C and redissolved in aHF (0.16 mL) at −78 °C. The solution was pumped to dryness at −76 °C over a period of 10 h to yield $[C_6F_5XeF_2][BF_4]\cdot 2HF$ as bright yellow, rhombohedral crystals. The crystal that was mounted had the dimensions of 0.22 × 0.49 × 0.13 mm^3.

*(iii) $[C_6F_5XeF_2][BF_4]\cdot 1.5NCCH_3$ (**3**).* On a glass vacuum line, CH_3CN (ca. 1 mL) was condensed at −196 °C onto a suspension of $[C_6F_5XeF_2][BF_4]$ (ca. 100 mg, 0.24 mmol) in CH_2Cl_2 (0.6 mL) to give a yellow solution at −60 °C. The reactor was then slowly cooled to −78 °C over a period of 6 h and placed in a −78 °C bath for 48 h. During this time period, CH_3CN crystallized, and small yellow crystals of $[C_6F_5XeF_2][BF_4]\cdot 1.5NCCH_3$ were formed within the crystalline CH_3CN mass. The remaining supernatant was removed through a 1.5 mm o.d. PTFE cannula as previously described.[40] Crystals of $[C_6F_5XeF_2][BF_4]\cdot 1.5NCCH_3$ were selected from the bulk solid mixture under a flow of dry, cold nitrogen. The crystal that was mounted had the dimensions 0.17 × 0.15 × 0.06 mm^3.

(b) Crystal Mounting and X-ray Data Collection. The mounted crystal was centered on a SMART APEX II diffractometer, equipped with an APEX II 4K charge-coupled device (CCD) and a triple-axis goniometer, controlled by the APEX2 Graphical User Interface (GUI) software.[80] A Bruker Triumph curved crystal monochromator with a Mo Kα source (λ = 0.710 73 Å) was used. The diffraction data collections consisted of: (**1**) ω scans (6204 frames) collected at 0.5° intervals at fixed χ = 54.7361°, (**2**) ω scans (9712 frames) and ϕ scans (1440) all collected at 0.5° intervals at fixed χ = 54.7361°, and (**3**) ω scans (3340 frames) collected at 0.5° intervals at fixed χ = 54.7361°. The crystal-to-detector distances were 4.954 cm for $[C_6F_5XeF_2][BF_4]$, $[C_6F_5XeF_2][BF_4]\cdot 2HF$, and $[C_6F_5XeF_2][BF_4]\cdot 1.5CH_3CN$, and the data collections were carried out in a 512 × 512 pixel mode using 2 × 2 pixel binning. All diffraction data were processed by use of the APEX2 GUI software,[80] which applied Lorentz and polarization corrections to three-dimensionally integrated diffraction spots. For $[C_6F_5XeF_2][BF_4]\cdot 2HF$ and $[C_6F_5XeF_2][BF_4]\cdot 1.5CH_3CN$, the processing of the raw data was straightforward and was completed using SAINT+,[81] which applied Lorentz and polarization corrections to three-dimensionally integrated diffraction spots. The program SADABS[82] was used for the scaling of diffraction data, the application of decay corrections, and empirical absorption corrections on the basis of the intensity ratios of redundant reflections. For $[C_6F_5XeF_2][BF_4]$, a preliminary solution was obtained (vide infra), but gave rise to a wR_2 value that was too high (~20%). The analysis of 1678 reflections with CELL_NOW[83] revealed the existence of two domains (~1323/332 reflections), the second domain being rotated with respect to the first domain by 178.6° about the reciprocal axis, 0.034, 1.000, 0.015. The raw data were processed using the multicomponent version of SAINT[81] under control of the two-component orientation file generated by CELL_NOW. The program TWINABS[84] was then used to generate different *hkl* files; the best R_{int} was obtained by fitting the first and largest domain separately as well as composite reflections that contained at least one contribution from the first domain.

(c) Solution and Refinement of the Structure. The XPREP[85] program was used to confirm the unit cell dimensions and the crystal lattices. The solutions were obtained by direct methods, which located the positions of the heavy atoms. The final refinement was obtained by introducing anisotropic thermal parameters and the recommended weightings for all of the atoms except the hydrogen atoms. In the case of $[C_6F_5XeF_2][BF_4]\cdot 1.5CH_3CN$, the H atoms bonded to the carbon atoms of the CH_3CN molecules were placed in calculated positions (C−H = 0.980 Å), whereas in the case of $[C_6F_5XeF_2][BF_4]\cdot 2HF$, the H atoms of the HF molecules were placed at locations derived from a difference map, and no restrictions were applied to the H−F bonds. In both cases, the H atoms were included as riding contributions with isotropic displacement parameters that were 1.2 times those of the attached atoms. In all three cases, the maximum electron densities in the final difference Fourier maps were located near the heavy atoms. The PLATON program[86] could not suggest additional or alternative symmetries. All calculations were performed using the SHELXTL-plus package[85] for the structure determinations, solution refinements, and molecular graphics.

Calculations. The optimized geometries and vibrational frequencies of $[C_6F_5XeF_2]^+$, $[C_6F_5XeF_2]^+\cdot NCCH_3$, $[C_6F_5XeF_2]^+\cdot 2NCCH_3$, $[C_6F_5XeF_2][BF_4]$, $C_6F_5IF_2$, $[C_6F_5Xe]^+$, $[C_6F_5Xe]^+\cdot NCCH_3$, C_6F_5I, C_6F_6, $[XeF_3]^+$, IF_3, $[XeF]^+$, IF, $[BF_4]^-$, and CH_3CN were calculated at the B3LYP and PBE1PBE levels of theory using aug-cc-pVTZ for H, B, C, N, and F, and aug-cc-pVTZ-(PP) for the I and Xe basis sets.[87] Quantum-chemical calculations were carried out using the program Gaussian 09[88] for geometry optimizations and vibrational frequencies and intensities. The program GaussView[89] was used to visualize the vibrational displacements that form the basis for the vibrational mode descriptions given in Tables 4 and 5 and Supporting Information, Tables S7, S9, and S10. Natural bond orbital analyses were performed using B3LYP and PBE1PBE densities with the NBO program (version 6.0).[63]

■ ASSOCIATED CONTENT

Ⓢ Supporting Information

Complementary discussion of the electrophilic fluorination properties of $[C_6F_5XeF_2][BF_4]$; the ^{19}F NMR spectrum of the $[BF_4]^-$ anion in $[C_6F_5XeF_2][BF_4]$ (aHF, −40 °C) (Figure S1); the ^{19}F and ^{129}Xe NMR spectra of $[C_6F_5XeF_2][BF_4]$ (aHF, −80 °C) (Figure S2); the experimental and calculated ^{19}F NMR spectra of $C_6F_5IF_2$ (CH_2Cl_2, 24 °C) (Figure S3); a comparison of NMR parameters for $[C_6F_5XeF_2][BF_4]$, $C_6F_5IF_2$, and $[C_6F_5Xe][BF_4]$ (Table S1); discussion of the ^{19}F NMR spectrum of $[BF_4]^-$ in $[C_6F_5XeF_2][BF_4]$ (−40 °C, aHF); complete list of experimental geometrical parameters for $[C_6F_5XeF_2][BF_4]$, $[C_6F_5XeF_2][BF_4]\cdot 2HF$, and $[C_6F_5XeF_2][BF_4]\cdot 1.5CH_3CN$ (Table S2); the unit cell of $[C_6F_5XeF_2][BF_4]$ showing the crystal packing viewed along the *a*-axis (Figure S4); complete Raman spectra of $[C_6F_5XeF_2][BF_4]$ (Figure S5) and $[C_6F_5XeF_2][BF_4]\cdot 2HF$ (Figure S6); factor-group analyses for $[C_6F_5XeF_2][BF_4]$ (Table S3) and $[C_6F_5XeF_2][BF_4]\cdot 2HF$ (Table S4); complete list of calculated geometrical parameters for $[C_6F_5XeF_2][BF_4]$, $[C_6F_5XeF_2][BF_4]\cdot 2HF$, $[C_6F_5XeF_2]^+\cdot 2CH_3CN$, $[C_6F_5XeF_2]^+$, and $C_6F_5IF_2$ (Table S5); calculated geometrical parameters for $[C_6F_5XeF_2]^+\cdot CH_3CN$ (Table S6); calculated geometry of $[C_6F_5XeF_2]^+\cdot CH_3CN$ (Figure S7); calculated vibrational frequencies for $[C_6F_5XeF_2]^+\cdot CH_3CN$, $[C_6F_5XeF_2]^+\cdot 2CH_3CN$, and CH_3CN (Table S7); calculated geometrical parameters for $[C_6F_5Xe]^+$ and C_6F_5I (Table S8); calculated geometries of $[C_6F_5Xe]^+$ and C_6F_5I (Figure S8); calculated vibrational frequencies and intensities for $[C_6F_5Xe]^+$ and C_6F_5I (Table S9); calculated geometrical parameters and the vibrational frequencies and intensities for $[XeF_3]^+$ and IF_3 (Table S10), $[XeF]^+$ and IF (Table S11) and $[BF_4]^-$ (Table S12); calculated natural atomic charges, Mayer bond orders, and Mayer natural atomic orbital valencies for $[C_6F_5XeF_2]^+$, $[C_6F_5XeF_2]^+\cdot CH_3CN$, $[C_6F_5XeF_2]^+\cdot 2CH_3CN$, $[C_6F_5XeF_2][BF_4]$, $[C_6F_5XeF_2][BF_4]\cdot 2HF$, $C_6F_5IF_2$, $[C_6F_5Xe]^+$, $[C_6F_5Xe]^+\cdot CH_3CN$, C_6F_5I, C_6F_6, $[XeF_3]^+$, IF_3, $[XeF]^+$, IF, CH_3CN, $[BF_4]^-$, and HF (Tables S13 and S14); energies and molecular orbitals of $C_6F_5IF_2$ (Figure S9). The X-ray crystallographic files in CIF format for the structure determinations of $[C_6F_5XeF_2][BF_4]$, $[C_6F_5XeF_2][BF_4]\cdot 2HF$,

dx.doi.org/10.1021/ic501831j | Inorg. Chem. XXXX, XXX, XXX−XXX

and $[C_6F_5XeF_2][BF_4]\cdot 1.5CH_3CN$. This material is available free of charge via the Internet at http://pubs.acs.org.

AUTHOR INFORMATION

Corresponding Authors

*E-mail: schrobil@mcmaster.ca (G.J.S.).
*E-mail: h.j.frohn@gmx.de (H.-J.F.).

Present Address

[§]Department of Inorganic and Structural Chemistry, Heinrich-Heine-Universität Düsseldorf, Universitätsstraße 1, 40225 Düsseldorf, Germany.

Author Contributions

[⊥]These authors contributed equally to the manuscript.

Notes

The authors declare no competing financial interest.

ACKNOWLEDGMENTS

This paper is dedicated to Prof. Dr. Boris Žemva on the occasion of his 75th birthday (June 8, 2015). We thank the Natural Sciences and Engineering Research Council of Canada for support in the form of a Discovery Grant (G.J.S.), the Deutsche Forschungsgemeinschaft and the Fonds der Chemischen Industrie for support in the form of research grants (H.-J.F.), the Ontario Ministry of Training, Colleges, and Universities for graduate scholarships (J.H.), and SHARCNet (Shared Hierarchical Academic Research Computing Network; www.sharcnet.ca) for computational resources.

REFERENCES

(1) Claassen, H. H.; Chernick, C. L.; Malm, J. G. *J. Am. Chem. Soc.* **1963**, *85*, 1927−1928.
(2) Schumacher, G. A.; Schrobilgen, G. J. *Inorg. Chem.* **1984**, *23*, 2923−2929.
(3) Levy, H. A.; Burns, J. H.; Agron, P. A. *Science* **1963**, *139*, 1208−1209.
(4) Gillespie, R. J.; Landa, B.; Schrobilgen, G. J. *Chem. Commun.* **1971**, 1543−1542.
(5) Boldrini, P.; Gillespie, R. J.; Ireland, P. R.; Schrobilgen, G. J. *Inorg. Chem.* **1974**, *13*, 1690−1694.
(6) McKee, D. E.; Zalkin, A.; Bartlett, N. *Inorg. Chem.* **1973**, *12*, 1713−1717.
(7) Christe, K. O.; Curtis, E. C.; Dixon, D. A.; Mercier, H. P.; Sanders, J. C. P.; Schrobilgen, G. J. *J. Am. Chem. Soc.* **1991**, *113*, 3351−3361.
(8) Brock, D. S.; Bilir, V.; Mercier, H. P. A.; Schrobilgen, G. J. *J. Am. Chem. Soc.* **2007**, *129*, 3598−3611.
(9) Ogden, J. S.; Turner, J. J. *Chem. Commun.* **1966**, *19*, 693−694.
(10) Jacob, E.; Opferkuch, R. *Angew. Chem., Int. Ed. Engl.* **1976**, *15*, 158−159.
(11) Gillespie, R. J.; Schrobilgen, G. J. *Chem. Commun.* **1977**, 595−597.
(12) Brock, D. S.; Mercier, H. P. A.; Schrobilgen, G. J. *J. Am. Chem. Soc.* **2010**, *132*, 10935−10943.
(13) Brock, D. S.; Schrobilgen, G. J. *J. Am. Chem. Soc.* **2011**, *133*, 6265−6269.
(14) Jacob, E.; Lentz, D.; Seppelt, K.; Simon, A. *Z. Anorg. Allg. Chem.* **1981**, *472*, 7−25.
(15) Turowsky, L.; Seppelt, K. *Z. Anorg. Allg. Chem.* **1992**, *609*, 153−156.
(16) Syvret, R. G.; Mitchell, K. M.; Sanders, J. C. P.; Schrobilgen, G. J. *Inorg. Chem.* **1992**, *31*, 3381−3385.
(17) Syvret, R. G.; Schrobilgen, G. J. *J. Chem. Soc. Chem. Commun.* **1985**, 1529−1530.
(18) Tavčar, G.; Žemva, B. *Angew. Chem., Int. Ed.* **2009**, *48*, 1432−1434.
(19) Brock, D. S.; Schrobilgen, G. J.; Žemva, B. Noble-Gas Chemistry. In *Comprehensive Inorganic Chemistry II;* Reedijk, J., Poepplemeier, K., Eds.; Elsevier: Oxford, U.K., 2013; Vol. *1*, Chapter 1.25, pp 755−822.
(20) Brock, D. S.; Mercier, H. P. A.; Schrobilgen, G. J. *J. Am. Chem. Soc.* **2013**, *135*, 5089−5104.
(21) Frohn, H.-J.; Bardin, V. V. *Organometallics* **2001**, *20*, 4750−4762.
(22) Frohn, H.-J.; Bardin, V. V. Organoxenonium Salts: Synthesis by Xenodeborylation, Reactivities, and NMR Spectroscopic Properties. In *Recent Developments in Carbocation and Onium Ion Chemistry;* Laali, K. K., Ed.; ACS Symposium Series 965; American Chemical Society: Washington, DC., 2007; pp 428−457.
(23) Tyrra, W.; Naumann, D. Organoxenon Compounds. In *Inorganic Chemistry Highlights;* Meyer, G., Naumann, D., Wesemann, L., Eds.; Wiley−VCH: Weinheim, Germany, 2002; pp 297−316.
(24) Frohn, H.-J.; Bardin, V. V. *J. Chem. Soc., Chem. Commun.* **1993**, 1072−1074.
(25) Frohn, H.-J.; Bardin, V. V. *Z. Anorg. Allg. Chem.* **2003**, *629*, 2465−2469.
(26) Frohn, H.-J.; Adonin, N. Y.; Bardin, V. V. *Z. Anorg. Allg. Chem.* **2003**, *629*, 2499−2508.
(27) Frohn, H.-J.; Bardin, V. V. *Chem. Commun.* **2003**, 2352−2353.
(28) Frohn, H.-J.; Bardin, V. V. *Eur. J. Inorg. Chem.* **2006**, 3948−3953.
(29) Zhdankin, V. V.; Stang, P. J.; Zefirov, N. S. *J. Chem. Soc., Chem. Commun.* **1992**, 578−579.
(30) Frohn, H.-J.; Theißen, M. *Angew. Chem., Int. Ed.* **2000**, *39*, 4591−4593.
(31) Frohn, H.-J.; Theißen, M. *J. Fluorine Chem.* **2004**, *125*, 981−988.
(32) Maggiarosa, N.; Naumann, D.; Tyrra, W. *Angew. Chem., Int. Ed.* **2000**, *39*, 4588−4591.
(33) Bock, H.; Hinz-Hübner, D.; Ruschewitz, U.; Naumann, D. *Angew. Chem., Int. Ed.* **2002**, *41*, 448−450.
(34) Frohn, H.-J.; Schroer, T.; Henkel, G. *Angew. Chem., Int. Ed.* **1999**, *38*, 2554−2556.
(35) Bilir, V.; Frohn, H.-J. *Acta Chim. Slov.* **2013**, *51*, 505−512.
(36) Frohn, H.-J.; Bilir, V.; Westphal, U. *Inorg. Chem.* **2012**, *51*, 11251−11258.
(37) Bartlett, N.; Sladky, F. O. *J. Am. Chem. Soc.* **1968**, *90*, 5316−5317.
(38) Frohn, H.-J.; LeBlond, N.; Lutar, K.; Žemva, B. *Angew. Chem., Int. Ed.* **2000**, *39*, 391−393.
(39) Zollinger, H. *Diazo Chemistry I; Aromatic and Heteroatomic Compounds;* VCH Verlagsgesellshaft mbH: Weinheim, Germany, 1994.
(40) Koppe, K.; Bilir, V.; Frohn, H.-J.; Mercier, H. P. A.; Schrobilgen, G. J. *Inorg. Chem.* **2007**, *46*, 9425−9437.
(41) Frohn, H.-J.; Hirschberg, M. E.; Westphal, U.; Flörke, U.; Boese, R.; Bläser, D. *Z. Anorg. Allg. Chem.* **2009**, *635*, 2249−2257.
(42) Bailly, F.; Barthen, P.; Breuer, W.; Frohn, H.-J.; Giesen, M.; Helber, J.; Henkel, G.; Priwitzer, A. *Z. Anorg. Allg. Chem.* **2000**, *626*, 2249−2257.
(43) Budzelaar, P. H. M. *gNMR,* 5.0.5; Adept Scientific plc: Oxford, U.K., 1999.
(44) Santry, D. P.; Mercier, H. P. A.; Schrobilgen, G. J. *ISOTOPOMER, A Multi-NMR Simulation Program,* version 3.02NTF; Snowbird Software, Inc.: Hamilton, Ontario, Canada, 2000.
(45) Pushkina, L. N.; Stepanov, A. P.; Zhukov, V. S.; Naumov, A. D. *Org. Magn. Reson.* **1972**, *4*, 607−623.
(46) Koppe, K.; Frohn, H.-J.; Mercier, H. P. A.; Schrobilgen, G. J. *Inorg. Chem.* **2008**, *47*, 3205−3217.
(47) Brunton, G. *Acta. Crystallogr., Sect. B* **1969**, *25*, 2161−2162.
(48) Boldrini, P.; Gillespie, R. J.; Ireland, P. R.; Schrobilgen, G. J. *Inorg. Chem.* **1974**, *13*, 1690−1694.
(49) Bondi, A. *J. Phys. Chem.* **1964**, *68*, 441−451.
(50) Frohn, H.-J.; Jakobs, S.; Henkel, G. *Angew. Chem., Int. Ed. Engl.* **1989**, *28*, 1506−1507.
(51) Steele, D.; Whiffen, D. H. *Spectrochim. Acta* **1960**, *17*, 368−375.

(52) Steele, D.; Whiffen, D. H. *Trans. Faraday Soc.* **1959**, *55*, 369−376.
(53) Long, D. A.; Steele, D. *Spectrochim. Acta* **1963**, *19*, 1947−1954.
(54) Long, D. A.; Steele, D. *Spectrochim. Acta* **1963**, *19*, 1955−1961.
(55) Hyams, I. J.; Lippincott, E. R. *Spectrochim. Acta* **1966**, *22*, 695−702.
(56) Bates, J. B.; Quist, A. S. *Spectrochim. Acta* **1975**, *31*, 1317−1327.
(57) Carter, R. L. *J. Chem. Educ.* **1971**, *48*, 297−303.
(58) Gillespie, R. J.; Landa, B.; Schrobilgen, G. J. *Inorg. Chem.* **1976**, *15*, 1256−1263.
(59) Claassen, H. H.; Chernick, C. L.; Malm, J. G. *J. Am. Chem. Soc.* **1963**, *85*, 1927−1928.
(60) Tsao, P.; Cobb, C. C.; Claassen, H. H. *J. Chem. Phys.* **1971**, *54*, 5247−5253.
(61) Naumann, D.; Rank, E.; Lehmann, E. *J. Fluorine Chem.* **1977**, *10*, 395−403.
(62) Schmeisser, M.; Naumann, D.; Lehmann, E. *J. Fluorine Chem.* **1973**, *3*, 441−444.
(63) Glendening, E. D.; Badenhoop, J. K.; Reed, A. E.; Carpenter, J. E.; Bohmann, J. A.; Morales, C. M.; Landis, C. R.; Weinhold, F. *NBO 6.0, Theoretical Chemistry Institute;* University of Wisconsin: Madison, WI, 2013.
(64) Casteel, W. J., Jr.; Dixon, D. A.; Mercier, H. P. A.; Schrobilgen, G. J. *Inorg. Chem.* **1996**, *35*, 4310−4322.
(65) Winfield, J. M. *J. Fluorine Chem.* **1984**, *25*, 91−98.
(66) Schrobilgen, G. J.; Holloway, J. H.; Granger, P.; Brevard, C. *Inorg. Chem.* **1978**, *17*, 980.
(67) Emara, A. A. A.; Schrobilgen, G. J. *Inorg. Chem.* **1992**, *31*, 1323−1332.
(68) Ignat'ev, N.; Sartori, P. *J. Fluorine Chem.* **2000**, *103*, 57−61.
(69) Chernick, C. L.; Malm, J. G. *Inorg. Synth.* **1966**, *8*, 254−258.
(70) Wall, L. A.; Donadio, R. E.; Pummer, W. J. *J. Am. Chem. Soc.* **1960**, *82*, 4846−4848.
(71) Fild, M.; Glemser, O.; Christoph, G. *Angew. Chem.* **1964**, *76*, 953.
(72) Royo, P.; Uson, R. *Rev. Acad. Cienc. Zaragoza (2)* **1969**, *24*, 119−122.
(73) Schmuck, A.; Seppelt, K. *Chem. Ber.* **1989**, *122*, 803−808.
(74) Frohn, H.-J.; Franke, H.; Fritzen, P.; Bardin, V. V. *J. Organomet. Chem.* **2000**, *598*, 127−135.
(75) Bertolini, J. C. *J. Emerg. Med.* **1992**, *10*, 163−168.
(76) Peters, D.; Miethchen, R. *J. Fluorine Chem.* **1996**, *79*, 161−165.
(77) Segal, E. B. *Chem. Health Saf.* **2000**, *7*, 18−23.
(78) Gerken, M.; Schrobilgen, G. J. *Coord. Chem. Rev.* **2000**, *197*, 335−395.
(79) Gerken, M.; Dixon, D. A.; Schrobilgen, G. J. *Inorg. Chem.* **2000**, *39*, 4244−4255.
(80) *APEX2,* release v2011.6−1; Bruker AXS, Inc.: Madison, WI, 1995.
(81) *SAINT+,* Version 6.02; Siemens Energy and Automation, Inc.: Madison, WI, 1999.
(82) Sheldrick, G. M. *Siemens Area Detector Absorption Corrections (SADABS),* Version 2.03; Bruker AXS, Inc.: Madison, WI, 1999.
(83) Sheldrick, G. M. *CELL-NOW,* University of Göttingen: Germany, 2008.
(84) Sheldrick, G. M. *TWINABS,* University of Göttingen: Germany, 2008.
(85) Sheldrick, G. M. *SHELXTL-Plus,* release 5.1; Siemens Analytical X-ray Instruments, Inc.; Madison, WI, 1998.
(86) Spek, A. L. *J. Appl. Crystallogr.* **2003**, *36*, 7−13.
(87) Basis sets and pseudopotentials were obtained from the Extensible Computational Chemistry Environment Basis set Database, version 2/25/04, as developed and distributed by the Molecular Science Computing Facility, Environmental and Molecular Science Laboratory, which is part of the Pacific Northwest Laboratory, P.O. Box 999, Richland, WA 99352.
(88) Frisch, M. J.; Trucks, G. W.; Schlegel, H. B.; Scuseria, G. E.; Robb, M. A.; Cheeseman, J. R.; Scalmani, G.; Barone, V.; Mennucci, B.; Petersson, G. A.; Nakatsuji, H.; Caricato, M.; Li, X.; Hratchian, H. P.; Izmaylov, A. F.; Bloino, J.; Zheng, G.; Sonnenberg, J. L.; Hada, M.; Ehara, M.; Toyota, K.; Fukuda, R.; Hasegawa, J.; Ishida, M.; Nakajima, T.; Honda, Y.; Kitao, O.; Nakai, H.; Vreven, T.; Montgomery, J. A., Jr.; Peralta, J. E.; Ogliaro, F.; Bearpark, M.; Heyd, J. J.; Brothers, E.; Kudin, K. N.; Staroverov, V. N.; Kobayashi, R.; Normand, J.; Raghavachari, K.; Rendell, A.; Burant, J. C.; Iyengar, S. S.; Tomasi, J.; Cossi, M.; Rega, N.; Millam, N. J.; Klene, M.; Knox, J. E.; Cross, J. B.; Bakken, V.; Adamo, C.; Jaramillo, J.; Gomperts, R.; Stratmann, R. E.; Yazyev, O.; Austin, A. J.; Cammi, R.; Pomelli, C.; Ochterski, J. W.; Martin, R. L.; Morokuma, K.; Zakrzewski, V. G.; Voth, G. A.; Salvador, P.; Dannenberg, J. J.; Dapprich, S.; Daniels, A. D.; Farkas, Ö.; Foresman, J. B.; Ortiz, J. V.; Cioslowski, J.; Fox, D. J. *Gaussian 09,* Revision D.01; Gaussian, Inc: Wallingford, CT, 2009.
(89) *GaussView,* release 3.0; Gaussian, Inc; Pittsburgh, PA, 2003.